An Observational and Modeling Study of the Processes Leading to Deep, Moist Convection in Complex Terrain

TAMMY M. WECKWERTH,* LINDSAY J. BENNETT,+ L. JAY MILLER,* JOËL VAN BAELEN,#
PAOLO DI GIROLAMO,@ ALAN M. BLYTH,+ AND TRACY J. HERTNEKY*

* *Earth Observing Laboratory, National Center for Atmospheric Research,& Boulder, Colorado*
+ *National Centre for Atmospheric Science, School of Earth and Environment, University of Leeds, Leeds, United Kingdom*
# *Laboratoire de Météorologie Physique, CNRS–Université Blaise Pascal, Clermont-Ferrand, France*
@ *Scuola di Ingegneria, Università degli Studi della Basilicata, Potenza, Italy*

(Manuscript received 2 July 2013, in final form 18 March 2014)

ABSTRACT

A case study of orographic convection initiation (CI) that occurred along the eastern slopes of the Vosges Mountains in France on 6 August 2007 during the Convective and Orographically-Induced Precipitation Study (COPS) is presented. Global positioning system (GPS) receivers and two Doppler on Wheels (DOW) mobile radars sampled the preconvective and storm environments and were respectively used to retrieve three-dimensional tomographic water vapor and wind fields. These retrieved data were supplemented with temperature, moisture, and winds from radiosondes from a site in the eastern Rhine Valley. High-resolution numerical simulations with the Weather Research and Forecasting (WRF) Model were used to further investigate the physical processes leading to convective precipitation.

This unique, time-varying combination of derived water vapor and winds from observations illustrated an increase in low-level moisture and convergence between upslope easterlies and downslope westerlies along the eastern slope of the Vosges Mountains. Uplift associated with these shallow, colliding boundary layer flows eventually led to the initiation of moist convection. WRF reproduced many features of the observed complicated flow, such as cyclonic (anticyclonic) flow around the southern (northern) end of the Vosges Mountains and the east-side convergent flow below the ridgeline. The WRF simulations also illustrated spatial and temporal variability in buoyancy and the removal of the lids prior to convective development. The timing and location of CI from the WRF simulations was surprisingly close to that observed.

1. Introduction

The Convective and Orographically-Induced Precipitation Study (COPS; Wulfmeyer et al. 2008, 2011) was designed to improve the forecasting skill of convective precipitation in complex terrain using observations and modeling of its life cycle. COPS was conducted 1 June–31 August 2007 with a variety of in situ and remote sensing instruments to sample clear air and moist convection. The region of southwestern Germany and eastern France was chosen because of its severe thunderstorm activity and low quantitative precipitation forecast (QPF) skill (Wulfmeyer et al. 2008). One of the critical components to achieving improved QPF skill is understanding the factors that influence the timing and location of new, deep, moist convection. This convection initiation (CI) problem is further complicated in regions of complex terrain.

Proper identification of the location and timing of CI and the associated precipitation is particularly important in mountainous regions where storms may or may not lead to flooding, depending upon which river catchments are affected (e.g., Rotach et al. 2009a, b). Inaccuracies in quantitative forecasts of mountain precipitation include the overestimation (underestimation) of precipitation on the windward (leeward)

& The National Center for Atmospheric Research is sponsored by the National Science Foundation.

Corresponding author address: Tammy M. Weckwerth, NCAR EOL, P.O. Box 3000, Boulder, CO 80307-3000.
E-mail: tammy@ucar.edu

DOI: 10.1175/MWR-D-13-00216.1

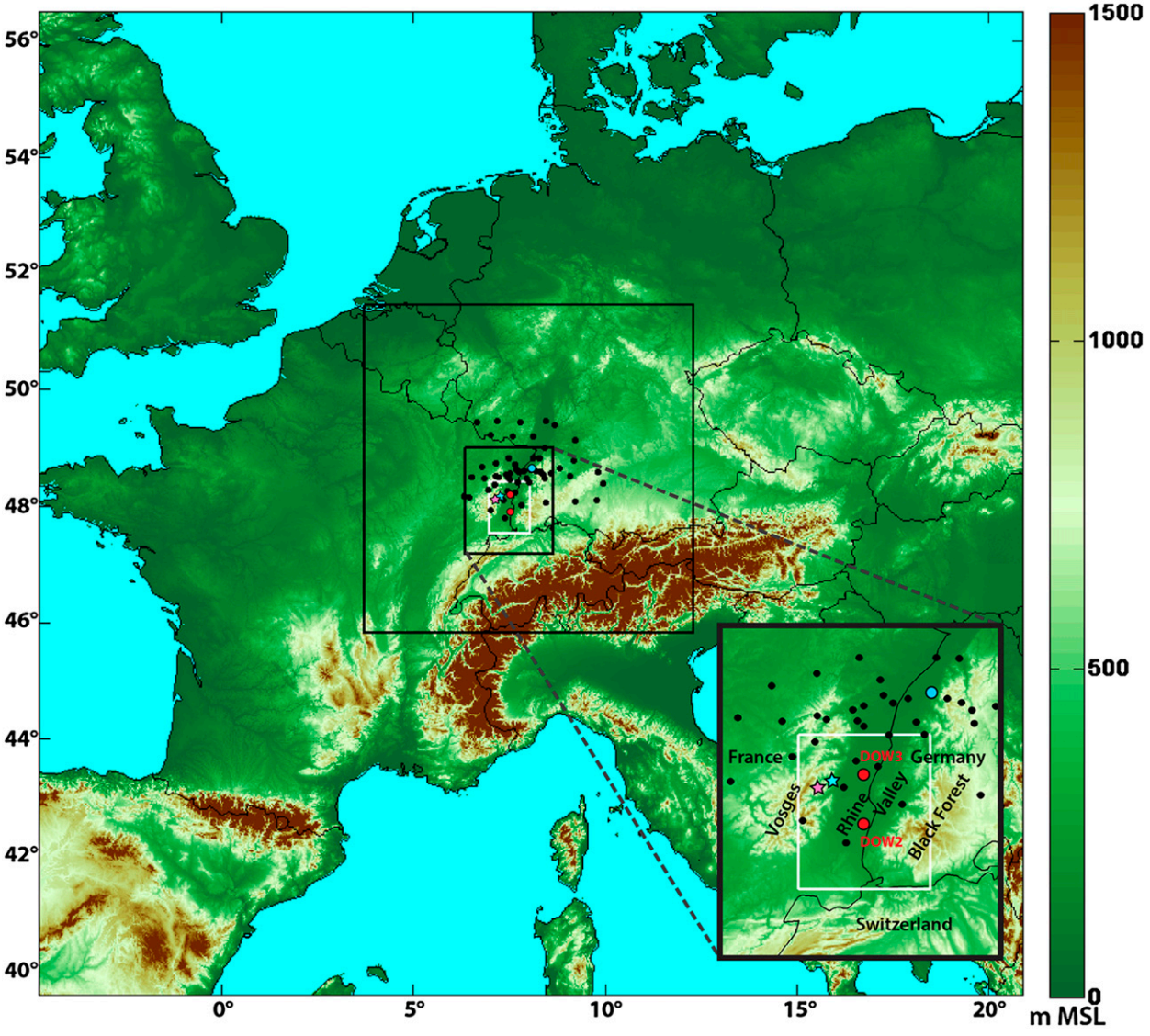

FIG. 1. COPS terrain-contoured base map showing locations of the three WRF domains (map size is outer domain). Shown are two black squares (with the innermost square also enlarged) that are the two WRF inner domains, dual-Doppler region to be shown in Fig. 11 (white square), GPS receivers (black dots), and DOW radar locations (red dots) on 6 Aug 2007. Supersite R (Achern; light blue dot) hosted the sounding system, wind profiler, and the BASIL Raman lidar. Light blue star is observed CI location; pink star is WRF simulated CI location.

side of the mountains and the production of phase errors in the diurnal cycle of precipitation. These phase errors in numerical models often produce precipitation several hours too early (e.g., Chaboureau et al. 2004).

Weckwerth et al. (2011) collected a climatology of CI events over a 9-yr period within the COPS domain, which included the Vosges Mountains, Rhine Valley, Black Forest Mountains, and Swabian Mountains. The latter mountains extend east of the inset shown in Fig. 1. The climatology showed that storms preferentially formed during the daytime along the mountain slopes and Rhine Valley. A possible explanation for the CI location and timing is that boundary layer convergence zones often formed and forced new deep, moist convection. In previous studies of nonsynoptically forced regions, low-level convergence zones have been shown to be preferred locations for convective development (e.g., Byers and Braham 1949; Purdom and Marcus 1982; Wilson and Schreiber 1986). These convergence zones may go undetected by the operational radar network due to substantial low-level blockage by trees and terrain and by the operational surface stations due to their wide spacing. Such low-level convergence, combined

with enhanced valley soil moisture (e.g., Kalthoff et al. 2011), may explain the frequent CI events in the valley. One such orographically induced convergence zone is the focus of this study.

Several COPS days illustrating the importance of low-level convergence in CI case studies have been examined in detail. For example, mountainous terrain commonly induces thermally driven circulations that lead to upslope flows that may influence CI via mesoscale convergence regions (e.g., Kottmeier et al. 2008). In a multiscale observational study of CI on 20 July 2007, Corsmeier et al. (2011) found that new storms occurred in advance of a gust front over the Black Forest. The interaction of orographic flow within the valleys of the Black Forest with the gust front, a mesoscale convergence line, and a synoptic-scale cold front led to the development of a squall line. Bennett et al. (2011) used Doppler on Wheels (DOW) radar data and Weather Research and Forecasting (WRF) Model simulations and further illustrated the importance of orographically induced convergence lines and gust fronts in the development of moderate convection on 12 August 2007. Hagen et al. (2011) compared and contrasted several COPS days with convection on the Vosges Mountains to days with convection in the lee of the mountains. They found that when the Froude number was low and the winds split around the Vosges Mountains, the thermally driven convergence at the ridge initiated convection. When the Froude number was high, the flow passed over the mountains and through the gaps and converged with the Rhine Valley flow to create optimal regions for CI in the valley. While the occurrence of low-level convergence zones helps to determine the preferred region of CI, all convergence boundaries do not cause CI.

Simulations of CI in the Black Forest Mountains illustrated the importance of background winds. For example, Hanley et al. (2011) found that strong westerlies enhanced CI potential by forcing moist air from the Rhine Valley up and over the Black Forest Mountain peaks. In contrast, Kirshbaum (2011) showed that strong background winds suppressed CI by weakening low-level convergence caused by differential heating and shortening the time that clouds could grow over their low-level convergence zone. This is consistent with observational results of Wilson and Megenhardt (1997), who showed that the correspondence between low-level convergence zone motion and the steering flow (e.g., 2–4 km above mean sea level or MSL; hereafter all heights are MSL) is essential for CI.

Additional remaining unknowns are the timing and exact location along the convergence zone where CI will occur. Thermodynamic information is often helpful information to combine with the wind fields. Van Baelen et al. (2011) used GPS data and tomographic retrievals, along with polarimetric Doppler radar (POLDIRAD) data on 15 July 2007, to show that enhanced water vapor on the crest of the mountains aided in ridge-top convection while increased water vapor, combined with local convergence in the Rhine Valley, produced convection over the plains. Similarly, Labbouz et al. (2013) found that enhanced moisture and convergence occurred prior to CI on 18 July 2007. They showed that small variations in the terrain also influenced the preferred CI locations. Behrendt et al. (2011) showed that storms formed on 15 July 2007 when a large-scale convergence zone was collocated with a thermally driven local convergence zone, creating enhanced low-level moisture flux convergence in the southern Black Forest and allowing the capping lids to be penetrated.

The 6 August 2007 case study presented in this paper evaluates the first-ever combination of high-resolution dual-Doppler wind fields with small-scale moisture fields, along with high-resolution WRF simulations, to show the combination of low-level winds, moisture, and buoyancy leading to CI. The radar radial velocity data were combined to obtain 3D wind fields and the GPS data were used to produce 3D moisture fields. This unique combination of winds and moisture allowed for the evaluation of moisture transport and accumulation prior to the initiation of convection. The WRF model was used in a nested high-resolution mode to simulate this case study and address the complicated kinematics and thermodynamics occurring on this day.

Section 2 will describe the COPS data and the relevant analysis methods and WRF simulations. Section 3 will present a synoptic and mesoscale overview of 6 August 2007 and provide WRF–observational comparisons. Section 4 will present details of the processes leading to CI. A summary and conclusions will be given in section 5.

2. Observational data and numerical simulations

a. Data and methods

This paper will focus on a subset of the extensive suite of COPS instruments. Meteosat Second Generation (MSG) 1-km visible satellite images were obtained every 15 min on 6 August 2007. The illustration of the cloud field development is a critical component for nowcasting CI (e.g., Wilson and Mueller 1993; Kingsmill 1995; Hane et al. 1987; May 1999). Composite radar displays were created every 10 min using the low-level scans from the German Weather Service (DWD) operational C-band radars. These composites were useful for illustrating the evolution of the storms once they formed, but they did not detect clear-air boundaries or early storms due to low-level radar blockage and elevated

radar beams at large distances. One of the DWD radars, Feldberg, observed the convection highlighted in this case study and will be shown. CI here is defined as the time precipitation formed and the radar echoes exceeded 30 dBZ.

The supersite at Achern on the eastern side of the Rhine River valley (Fig. 1) was equipped with radiosonde launching capabilities, a wind profiler and the University of Basilicata Raman lidar system (BASIL) that provided continuous vertical profiles of water vapor mixing ratio (Di Girolamo et al. 2009). Measurements of the water vapor mixing ratio are based on the application of the roto-vibrational Raman lidar technique in the ultraviolet region. In addition to water vapor, BASIL provides measurements of atmospheric temperature, particle backscatter at 355, 532, and 1064 nm, particle extinction at 355 and 532 nm, and particle depolarization at 355 and 532 nm (Di Girolamo et al. 2012). The BASIL water vapor profiles must be precalibrated with an independent measurement, such as soundings, GPS, or microwave radiometer measurements. For the purpose of this current study the precalibration was performed prior to operations on 6 August based on an extensive comparison of the water vapor mixing ratio profiles from BASIL with >100 simultaneous radiosonde profiles. The radiosondes were a combination of Vaisala RS80 and RS92 radiosondes. The moisture dry bias correction was applied to all RS80 radiosondes using the technique of Wang et al. (2002). The lidar calibration constant was determined by using BASIL and radiosonde profiles in the altitude region between 1 and 2 km. The consideration of more than 100 radiosonde profiles for the determination of the calibration constant prevents the dependence of a single lidar vertical profile upon the simultaneous radiosonde profile. The BASIL data used in this study were integrated over 15 min and have a vertical resolution of 150 m, starting at 150 m AGL. Through the application of Poisson statistics, the daytime water vapor precision (random error) was 5% at 2 km and 20% at 4 km (Bhawar et al. 2011). The systematic error affecting the BASIL measurements did not exceed 3%–5%. The resulting water vapor profiles were useful for comparison with the WRF simulations to aid in assessing the representativeness of the simulations.

GPS receivers are used worldwide for autonomous, all-weather, and continuous observations of integrated precipitable water vapor (PWV) along the path from the satellite to the ground-based receiver (e.g., Bevis et al. 1992, 1994; Businger et al. 1996). These quasi-vertical columns of PWV can be retrieved with high accuracy (e.g., Van Baelen et al. 2005; Wang et al. 2007). With a dense network of GPS receivers, a tomographic retrieval can be performed to obtain the three-dimensional moisture field (e.g., Van Baelen et al. 2011). The spacing of the 54 receivers in the COPS domain varied between 10 and 40 km (see Fig. 1 for station distribution), which is near the limit for performing high-quality tomographic retrievals. The tomographic retrievals provided a gridded moisture field with horizontal resolution of 18.5 km in the meridional direction and 15.9 km in the zonal direction. The vertical resolution was 500 m up to 4 km, increasing to 750 m up to 7 km and further increasing to 1 km up to 10 km. Processing to obtain PWV and 3D tomographic moisture fields was performed as in Van Baelen et al. (2011).

Two DOW mobile radars (Wurman et al. 1997) were positioned with a north–south-oriented 30.6-km baseline on 6 August to obtain high-resolution dual-Doppler wind measurements within the Rhine Valley and along the eastern and western slopes of the Vosges and Black Forest Mountains, respectively. Both DOWs are X-band (3 cm; ~9.4 GHz) Doppler radars that are sensitive to backscattering from insects, nearby clouds, and precipitation particles. The DOWs have 0.93° half-power beamwidths and were operated with 150-m range-gate spacing during COPS.

Once the radars were positioned early in the morning (with DOW3 to the north and DOW2 to the south) and leveled, solar scans were taken for aligning the azimuth angles with true north. The radars were operated with 0.5° azimuthal spacing in coordinated 360° surveillance scanning mode at several low-elevation angles from 1013 to 2116 UTC [hereinafter all times are UTC; UTC = central European summer time (CEST) − 2 h]. These constant-elevation-angle scans typically consisted of 10 angles (nominally 1°, 1.5°, 2°, 2.5°, 3°, 4°, 5°, 6.5°, 8°, and 10°) during synchronized ~2.5-min periods. Volumetric scanning sequences covered much of the southern Rhine Valley as well as the eastern slopes of the Vosges Mountains, whose ridgeline is oriented roughly along a northeast–southwest direction and whose maximum heights are ~1.5 km.

The mobile radar data were corrected for any pointing errors and carefully edited to remove noise, ground clutter, and second-trip echoes using the National Center for Atmospheric Research (NCAR) SOLO II software package (Oye et al. 1995). Edited data at spherical locations were mapped with the NCAR Reorder software onto a regular Cartesian grid with 500-m horizontal and 250-m vertical grid spacings. The lowest level of the grid was 0.25 km (~50 m above the floor of the Rhine Valley) and the highest level was 5 km. Cressman (1959) distance-weighted averages of all data points within nearby 0.5-km radius regions surrounding each of the output grid points were used. The 0.5-km radii were increased to 0.7 km beyond a 35-km range to ensure that

at least two and no more than three azimuths and two elevation angles were used in the mapping process. This approach ensured that each output grid point was well bounded by azimuth and elevation beams, included about seven range gates, and allowed the radial velocities to be treated as scalars. The number of radar measurements included for estimating output grid values varied from ~60 near the radars to ~30 at the farthest slant ranges.

The Custom Editing and Display of Reduced Information in Cartesian space (CEDRIC; Mohr et al. 1986) software package was used to perform the dual-Doppler wind synthesis (e.g., Miller et al. 1988, 1990). An examination of successive volumetric scans revealed that overall flow patterns changed only slowly and exhibited little or no advection. Therefore no time adjustments were made during the wind synthesis, a procedure first suggested by Gal-Chen (1982). Little or no intrinsic fall speeds of the air motion tracers or vertical air motions were likely to contaminate the radial velocity measurements because of the low elevation angles scanned by the radars. This dual-Doppler (or two-equation) solution was deemed to adequately represent the horizontal wind field. Before the winds were synthesized, each of the radial velocity datasets were edited in CEDRIC to remove some obvious outliers and to fill in some small holes using linear-least squares methods. Once radial data were cleaned up and filled, a two-dimensional Hanning filter was applied over 5×5 horizontal regions. Much of this more heavy-handed decimation, filling, and filtering was required to reduce some obvious measurement errors from ~(0.8–1.0) m s^{-1} to something nearer to ~(0.1–0.2) m s^{-1}. Before precipitation developed, relatively weak radar signal strength caused these large measurement errors. With maximum radial velocities of ~5 m s^{-1}, this amounts to a noise reduction from about 20% down to near 1%.

Vertical velocities were estimated from derived horizontal wind convergence using the O'Brien (1970) variational scheme applied to the anelastic mass continuity equation with boundary conditions of $w = 0$ both at the ground and at the top of the grid. This is roughly equivalent to allowing the lowest z-level convergence to represent a layer average between that level and the ground. During the pre-CI period near the top of the grid, radar echoes were consistently capped at ~4 km, indicating no echo or vertical motion above that level. Further two-dimensional Hanning filtering over horizontal 3×3 regions of convergence was used prior to vertical integration to eliminate noise amplification at twice the horizontal grid spacing that is inherent in centered finite-differencing schemes. Estimated errors in retrieved horizontal and vertical motions are no more than 0.1–0.2 m s^{-1}.

Surface station gridded analyses were derived using a mesoscale data analysis and downscaling method, named the Vienna Enhanced Resolution Analysis (VERA; e.g., Steinacker et al. 2000, 2006; Gorgas et al. 2009). VERA utilizes more than 12 000 Global Telecommunication System (GTS) and non-GTS surface station datasets to provide an 8-km gridded field every hour. The VERA technique calculates gridded fields of potential temperature, equivalent potential temperature, water vapor mixing ratio, mean sea level pressure, horizontal winds, and precipitation. These VERA fields will be used for comparison with the tomography, DOW winds, and WRF simulated fields, as well as a method for evaluating the large-scale surface conditions.

b. *WRF simulations*

The WRF Model version 3.1.1 (Skamarock et al. 2008) was used with two-way nested domains of 6.3-, 2.1-, and 0.7-km grid spacing and 121 vertical levels. The inner domain covered the Vosges Mountains, the Rhine Valley, and the western part of the Black Forest Mountains (Fig. 1). The simulation was initialized at 0000 by Global Forecast System (GFS) 1° analyses, which also provided the lateral boundary conditions updated every 6 h. A control simulation used the following subgrid parameterization schemes, described in Skamarock et al. (2008): Thompson microphysics, Dudhia shortwave radiation and Rapid Radiative Transfer Model (RRTM) longwave radiation, Mellor–Yamada–Janjic (MYJ) turbulent kinetic energy (TKE), Monin–Obukhov surface layer physics, and the Noah land surface model (LSM). The Noah LSM carries soil moisture and temperature at four levels. The Betts–Miller–Janjic cumulus parameterization scheme was applied on the outer 6.3-km domain only. A series of sensitivity studies were performed by varying the input analyses fields and parameterization schemes and showed that the simulation results were robust, all producing similar wind, cloud, and rain fields.

3. Overview of 6 August 2007

In this section, the broader-scale context will be described using weather maps, satellite imagery, and surface observations. These observations will be compared with the WRF outer domain simulations.

a. *Synoptic discussion*

At 1200 on 6 August 2007 there was a weak 500-hPa low pressure region over eastern Europe, an elongated ridge stretching from northern Africa through France and Germany to the Baltic Sea, and a deep trough extending from Iceland south to Ireland (not shown). At the surface a low pressure system was centered over northeast

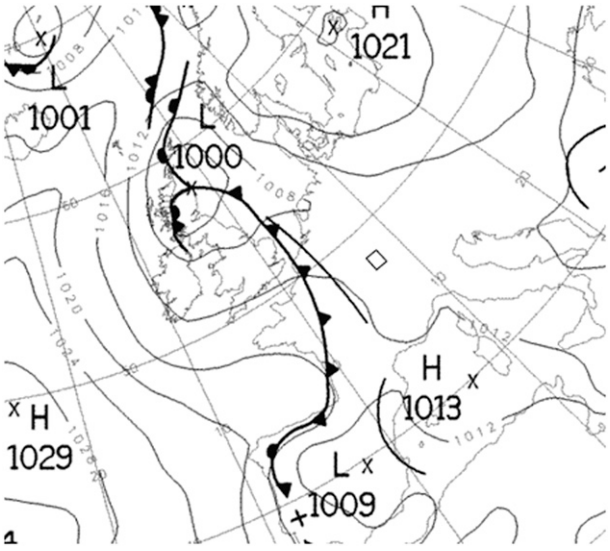

FIG. 2. Synoptic surface map at 1200 UTC 6 Aug 2007. Black square (just south of 50°N and west of 10°E) indicates the dual-Doppler radar domain to be shown in Fig. 11. The cold front approaching from the west is preceded by a trough line (black line). The ×s mark the low or high pressure locations with the L or H and associated number designating the pressure values in hPa. Chart courtesy of the Met Office.

Scotland with a weak cold front extending south over the North Sea, central France, and into northern Spain (Fig. 2). There was a narrow band of precipitation associated with this front, but deeper convection developed ahead of it during the morning, organizing into a north–south-oriented line by 1200. The clouds and precipitation were sandwiched between the cold front boundary and prefrontal trough of Fig. 2. The convection formed within an 850-mb (1 mb = 1 hPa) plume of high-θ_e air with its western boundary marked by the cold front. A prefrontal trough and convergence zone formed within this plume, perhaps in response to a 500-mb vorticity maximum moving northeastward over France. This slow-moving front and its associated precipitation remained west of the Vosges Mountains throughout the case study presented herein.

b. *Satellite and surface observations*

Hourly MSG visible satellite imagery showed a wide band of clouds and precipitation approaching the COPS region. The cloudiness in advance of the frontal-trough region was apparent along the western edge of the 1200 image (Fig. 3a). The GPS PWV overlaid on the visible satellite image showed a large-scale moisture gradient with moist air occurring east of the cloud field but west of the Vosges Mountains. As the synoptic-scale system slowly approached the COPS domain, there were some scattered shallow cumulus clouds along the eastern slopes of the Vosges Mountains at 1300 (Fig. 3b). These early clouds were in the region where the largest convective storms eventually developed. It is possible that these small convective clouds may have been instrumental in vertical mixing and moistening of the region prior to the formation of deeper convection. The PWV field suggested that the enhanced moisture ahead of the front also advected into the COPS domain, apparent by the higher PWV values in the Vosges Mountains and the western Rhine Valley. At 1400 a thin line of small cumulus formed along the Vosges Mountains within higher PWV air that had further advected from the west (Fig. 3c). The storms growing on the Vosges Mountains continued to develop by 1500 as the frontal-trough system continued its slow approach from the west (Fig. 3d). By 1600 the Vosges Mountains convection was among the strongest precipitation in the region as it formed an anvil and merged with the precipitation associated with the prefrontal trough (see Fig. 7d).

The VERA 8-km surface analyses showed cool (darker blues in Fig. 4, left panels), relatively dry air associated with the advancing frontal-trough system to the west of the COPS dual-Doppler box. The 1000 potential temperature field (Fig. 4a) also illustrated a broad warm region within and surrounding the dual-Doppler box with several hotter pockets along the peaks of the Black Forest Mountains and the Alps. These warm regions at higher elevations would be expected in a statically stable environment. In advance of the cold, dry front, a plume of moisture extended north-northeastward from the northwestern Mediterranean Sea through France west of the Vosges Mountains and northward to the Netherlands (Fig. 4b). This moisture east of the frontal-trough region was also observed in the PWV fields (Fig. 3). By 1200 the cool, moist prefrontal air advected eastward to just west of the Vosges Mountains, while the COPS region had warmed and moistened. Note that the area within the dual-Doppler box became warmer (more yellow; Fig. 4c) and moister (more blue; Fig. 4d) at 1200. At 1400 the cool air associated with the front and trough was pushed up against the western slope of the Vosges Mountains (Fig. 4e). The prefrontal moisture was distributed throughout the dual-Doppler box as the region continued to become moister (Fig. 4f) by the time of CI, which occurred at 1400.

c. *WRF–observation comparisons*

The 1400 visible satellite image (Fig. 5a) and the 1400 European composite radar image (Fig. 5b) respectively illustrate the cloud and moderate precipitation bands associated with the frontal-trough system. The location, extent, and timing of the front and associated clouds and rainfall were well represented within the WRF 6.3-km outer domain (Fig. 5c). As in the observations, the

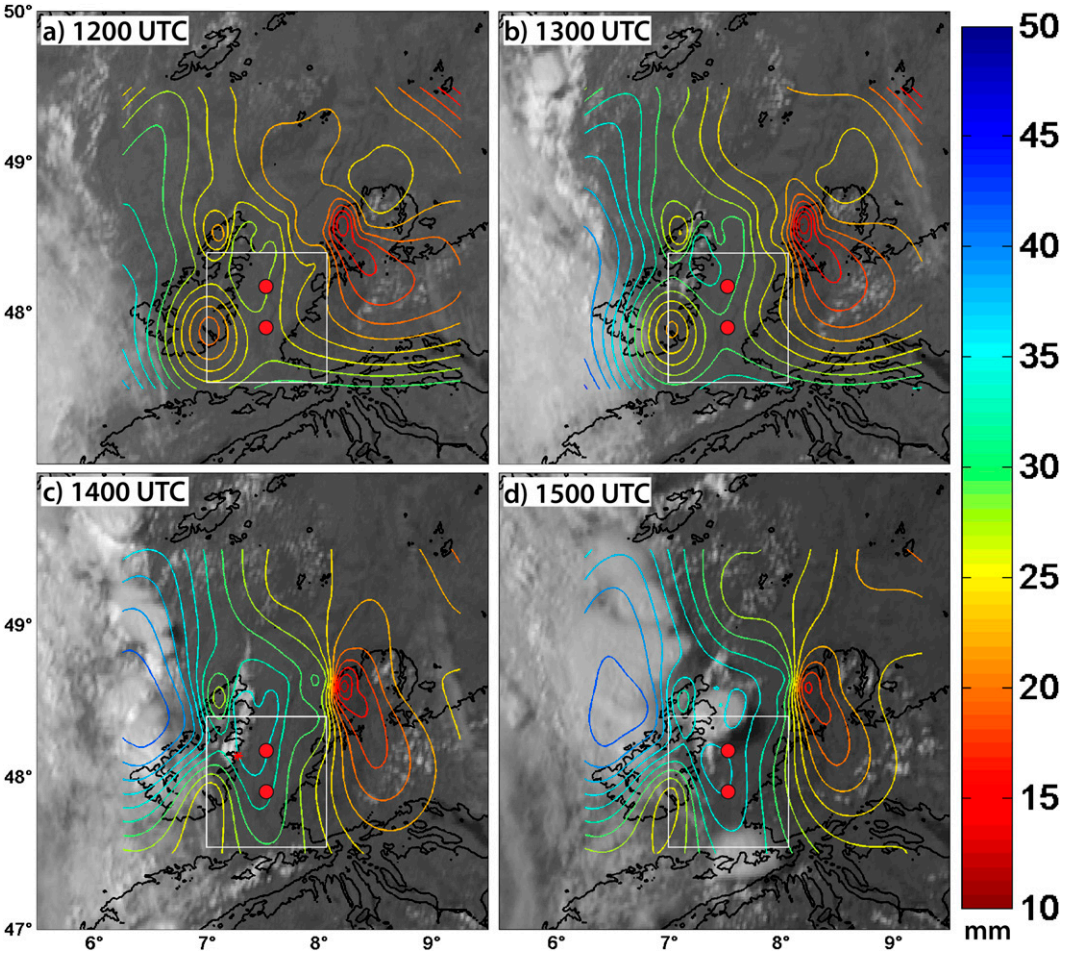

FIG. 3. Meteosat high-resolution visible satellite imagery from (a) 1200, (b) 1300, (c) 1400, and (d) 1500 UTC 6 Aug 2007. Colored contours are GPS PWV values in mm. The 500-m MSL terrain contour is shown in black. Red dots show the locations of the two DOW radars while the white square is the dual-Doppler region shown in Fig. 11. Red asterisk in (c) is the observed CI location.

simulation produced the frontal-trough cloud band west of the COPS region at 1400 with preceding clouds on the Vosges Mountains. While there was strong qualitative agreement, even small errors in the location of the simulated front could adversely affect the ensuing convective precipitation. In fact, some details of the WRF simulation inaccurately produced clouds and precipitation in the Alps and in the southeast portion of the COPS domain. In the simulations, however, precipitation formed along the Vosges Mountains by 1415, similar to that observed. The simulated storms that initiated on the Vosges Mountains were not as intense as the observed storms and they prematurely propagated into the Rhine Valley and dissipated (not shown). Nevertheless, the timing and location of the simulated and observed large-scale cloud and precipitation fields were similar, providing confidence in the WRF simulations for this case.

Various fields of the WRF 2.1-km inner domain compared favorably to the VERA 2-km analysis fields but are not shown for brevity. The WRF simulated surface winds were slightly stronger than the observed VERA wind field analysis, particularly in the north. The winds in the southern part of the domain were comparable in both speed and direction. The surface potential temperature difference was consistently within 2 K in the dual-Doppler region. The WRF simulations produced a too-high surface potential temperature on the highest peaks in the Black Forest Mountains and Vosges Mountains and in the Alps to the south. The mixing ratio comparisons were also reasonable with the WRF values consistently being within $2\,g\,kg^{-1}$ of VERA.

Figure 6 shows the sounding nearest to the region of CI. It was launched at 1400 from the Achern Supersite, which was 81 km away on the opposite side of the Rhine Valley (see Fig. 5 for relative locations). This sounding

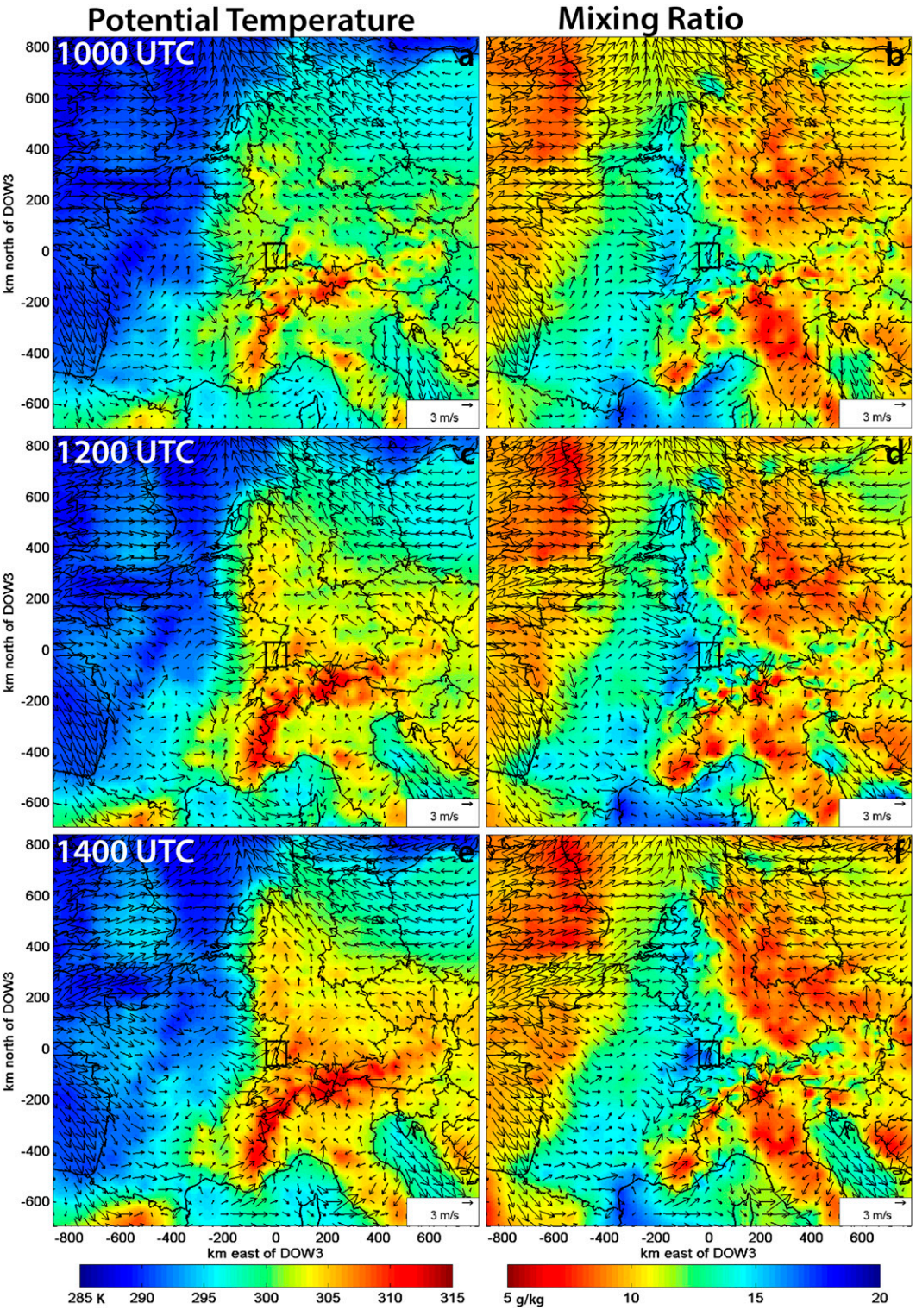

FIG. 4. VERA surface analyses of (left) potential temperature (K) and (right) mixing ratio ($g\,kg^{-1}$) with wind vectors ($m\,s^{-1}$) overlaid. Times shown are (top) 1000, (middle) 1200, and (bottom) 1400 UTC. Black square near center is dual-Doppler region to be shown in Fig. 11.

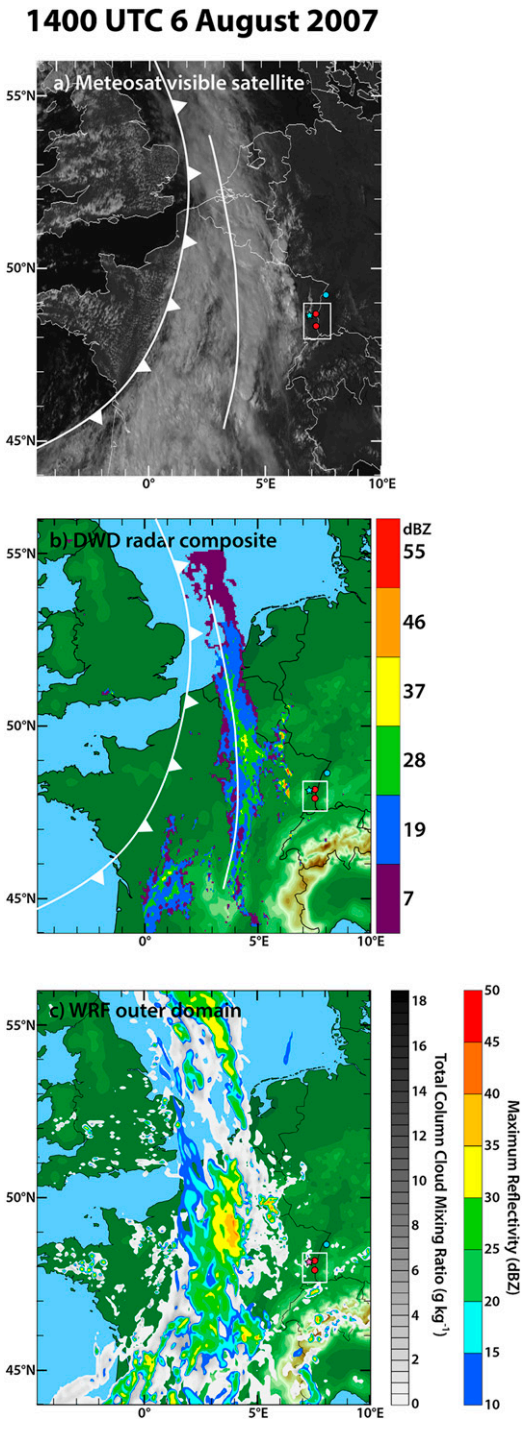

FIG. 5. Comparison of 1400 UTC 6 Aug 2007 (a) Meteosat visible satellite image, (b) DWD radar composite, and (c) WRF outer domain simulation. The cold front and trough locations in (a),(b) are approximated. White dual-Doppler box to be shown in Fig. 11 is shown in all panels as are red dots showing locations of DOW2 and DOW3. The Achern Supersite location is the blue dot in the northeastern Rhine Valley. Blue star is the CI location observed in (a),(b) and pink star is the WRF simulated CI location in (c). Colored shading is maximum radar reflectivity (dBZ): observed in (b) and simulated in (c). Gray shading in (c) is total column-integrated cloud water mixing ratios (g kg^{-1}).

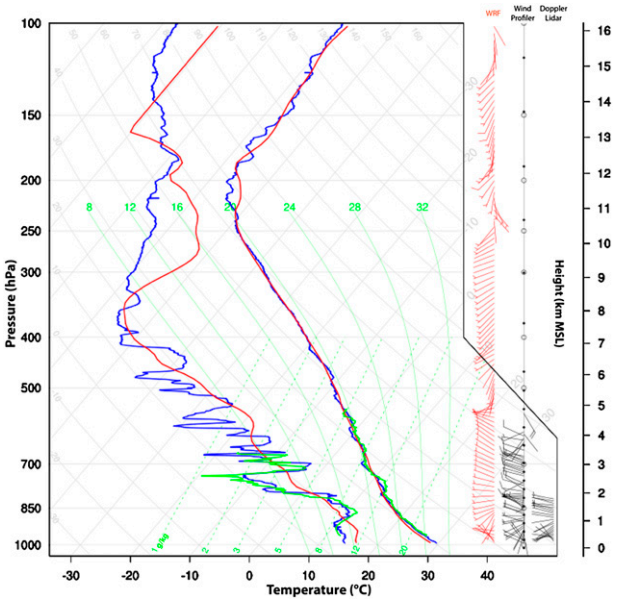

FIG. 6. Comparison between Achern radiosonde profile (blue) with the WRF simulated profile (red) at 1400 UTC 6 Aug 2007. The BASIL lidar moisture and temperature profiles are shown in green. The WRF wind profile (red) is also shown along with the Achern wind profiler and Doppler lidar wind profiles (both in black). Winds from the radiosonde were not recovered.

profile is useful to compare with the WRF simulations. In particular, the WRF temperature profile closely follows the Achern sounding and BASIL profiles in the boundary layer, through the cloud layer, and up to 100 hPa, including the identification of the height and strength of the tropopause. The radiosonde and BASIL lidar moisture profiles were similar in structure and magnitude up to 3.5 km. There was a dry layer from the surface up to 925 hPa topped by a shallow moist layer up to ~825 hPa. From 825 up to 700 hPa there was another dry layer that was bracketed by weak (1–2 K) temperature inversions. This combination may have prevented convective development through that layer at Achern. The WRF dewpoint temperature profile (and indeed the WRF temperature profile) captured neither the multiple layers nor the vertical variability observed by the radiosonde and BASIL, perhaps due to the vertical resolution of both the input analyses and the model itself. WRF results also showed too much moisture below 925 hPa followed by too little up to 825 hPa and greater moisture up to 725 hPa. The WRF profile between 330 and 200 hPa was again too moist but this high-level moisture was likely not impacting the low-level CI activity studied herein. Broadly speaking, the WRF moisture profile looks like a heavily smoothed, but similar, version of the observed profile, especially in the lower levels (1000–300 hPa).

The Achern sounding showed minimal convective available potential energy (CAPE) of 5 J kg^{-1} and a substantial amount of convective inhibition (CIN; −180 J kg^{-1}) with a level of free convection (LFC) of 4.8 km. These stability parameters were calculated assuming parcel ascent from the lowest 50-mb-averaged temperature and moisture values. Primarily owing to the WRF simulation's overprediction of low-level moisture at Achern at 1400, the WRF stability parameters were different than the observations (i.e., CAPE of 377 J kg^{-1}, CIN of −94 J kg^{-1}, and LFC of 3.0 km) but both the observations and simulations suggested limited CI potential at Achern. Indeed, convection was not initiated at the Achern site.

Winds were not retrieved by this sounding, so the wind profilers from two Achern instruments are shown: the U.K. National Centre for Atmospheric Science (NCAS) wind profiler and the University of Salford Doppler lidar. The WRF wind profile was consistent with the observed wind profiles up to 4 km.

There were some detailed and minor differences between the WRF and observed soundings. However, the fact that the main features of the 1400 Achern temperature, moisture, and wind profiles were all generally well reproduced in the WRF simulation justifies the use of WRF to extend the observational capabilities of this 6 August 2007 CI case study.

4. Convection initiation

A combination of radar, GPS tomography, and WRF 0.7-km inner domain simulation results will be used to evaluate the precursors to CI. A detailed model reproduction of the CI event will be presented in section 4b(2). The Feldberg radar reflectivity field showed no echoes at 1305 (Fig. 7a). Precipitation with radar reflectivities of 50 dBZ associated with the frontal-trough system was observed in northern France by 1400 (Fig. 7b). In advance of the front, two small, weak radar echoes formed on the eastern Vosges Mountains in the same region as the Meteosat clouds that were initially observed 1 h earlier (Fig. 3b). These represent the first radar echoes for the CI studied herein. By 1455 the echoes in this region merged into a small convective system that produced strong precipitation with reflectivities >50 dBZ along the slopes of the Vosges Mountains (Fig. 7c). An inspection of the more frequent Feldberg radar scans (not shown) showed that the synoptic-scale band of frontal-trough precipitation merged with the Vosges Mountains precipitation by 1600 as the entire system advected into the Rhine Valley (Fig. 7d).

a. Static stability and buoyancy

Figure 8 presents a skew T–log$p$ time series of the WRF soundings taken at the location of the first WRF precipitation echo (at the pink star in Figs. 1 and 5c). At 0800 there was substantial CIN (−320 J kg^{-1}) and minimal CAPE (26 J kg^{-1}) with an LFC at ~5.3 km. The winds were southwesterly below 2 km veering to westerly up to 4.5 km and then backing to southwesterly up to ~7 km.

The convective boundary layer (CBL) formed by 1000, apparent by nearly constant potential temperature and mixing ratio profiles up to ~1 km. The LFC descended to ~2.9 km, the CIN decreased to −78 J kg^{-1}, and the CAPE increased to 748 J kg^{-1}. There was a suggestion of low-level easterly flow as the differential heating allowed for upslope (anabatic) flow into the Vosges Mountains. Such mountain-valley anabatic flows are common (e.g., Banta 1984; Neiman et al. 2002; Geerts et al. 2008).

At 1200 the CBL was well mixed up to ~1.8 km, topped by a slight capping inversion creating a small amount of CIN of −17 J kg^{-1}. The LFC was 813 hPa (1.8 km) with a CAPE of 1228 J kg^{-1}. Easterly winds were clearly evident below ~1 km with westerly winds above. A continuing increase in midlevel moisture (800–500 hPa) may be attributed to large-scale ascent and/or moisture advection associated with the approaching front/trough system.

The sounding at 1400 showed a well-mixed ~1.8-km-deep CBL topped by a weak capping inversion and increase in CBL moisture. There was very little CIN (−2 J kg^{-1}), an LFC at ~1.5 km, and CAPE of 1800 J kg^{-1}. Although low-level winds were northeasterly, there remained a sufficient upslope component to collide with the westerly flow over the ridge top and maintain convergence along the slopes. This upslope–downslope flow continued to maintain a region conducive to convective development.

Overall, the simulated profiles at the CI location trended toward a more unstable environment characterized by an increase in boundary layer moisture and temperature, along with an increase in midlevel (800–500 hPa) moisture and a corresponding decrease in the midlevel temperature.

The WRF simulations were extended further to compare buoyancy and lids between the CI location and a non-CI grid point 6.4 km to the west along the ridgeline. The ridge top was chosen for the non-CI location because the Froude number calculated from the upstream operational sounding at Nancy, France, was 0.5 and presumably should have led to ridge-top CI (Hagen et al. 2011). Following the analyses performed with observational soundings by Morcrette et al. (2007), time–height plots of simulated wet-bulb potential temperatures (θ_w) were used to assess temporal and spatial bulk buoyancy potential and lid variations (Fig. 9). The quantity θ_w is the temperature to which a parcel of air at constant pressure cools through evaporation of water

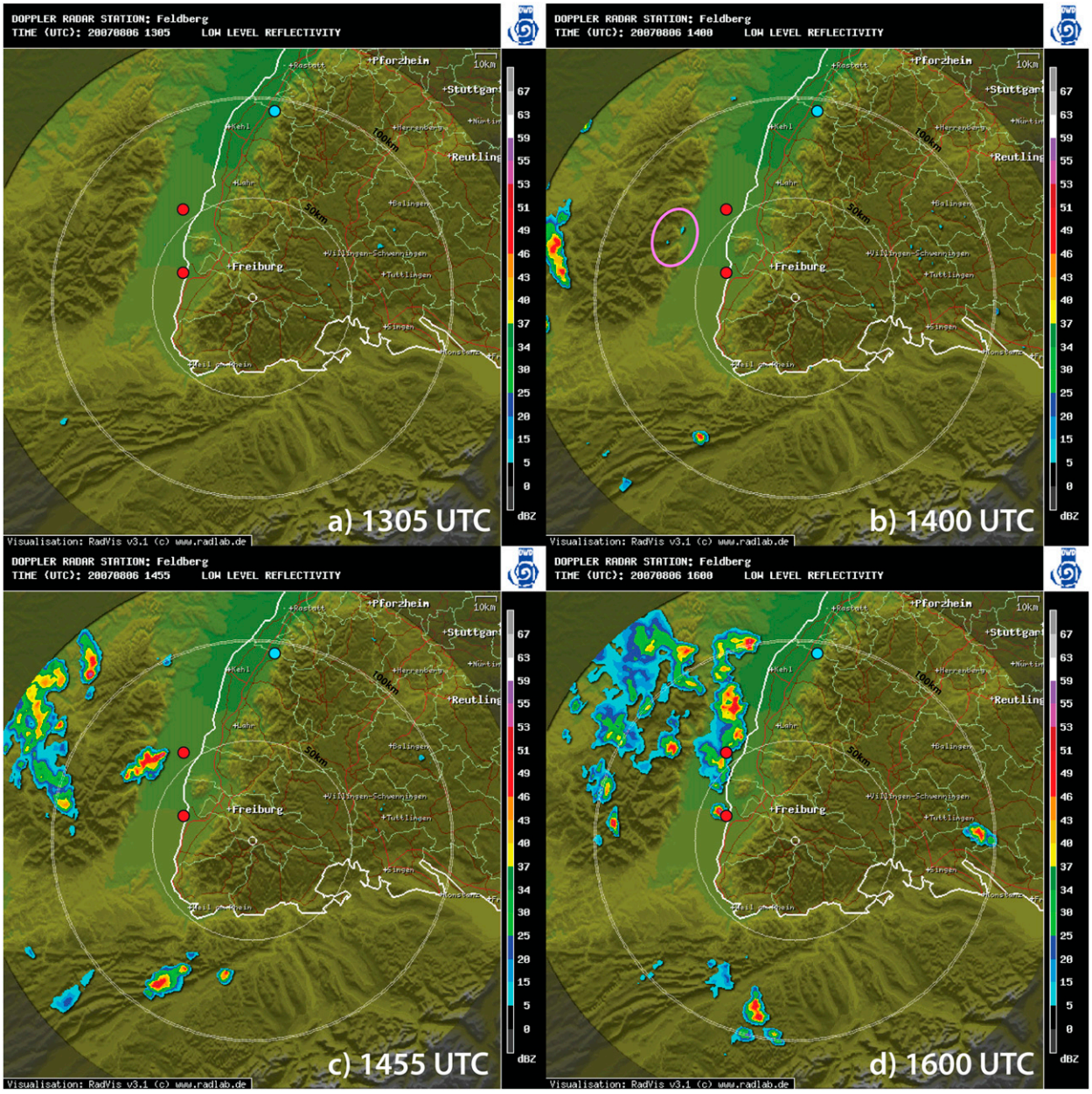

FIG. 7. Feldberg radar reflectivity (dBZ) images at (a) 1305, (b) 1400, (c) 1455, and (d) 1600 UTC 6 Aug 2007. Range rings are every 50 km. Red dots are the locations of DOW2 and DOW3, and the blue dot shows the Achern Supersite location. Pink circle in (b) shows the first radar echo that developed into deep convection. Within the Rhine Valley, the France–Germany border closely matches the Rhine River.

into it when it is brought moist adiabatically to 1000 hPa. Potential instability occurs when high θ_w air lies beneath low θ_w air. The color shadings illustrate the θ_w below the LCL and the saturation wet-bulb potential temperature (θ_{ws}) above the LCL (thick black line). At the simulated CI location at 669 m (Fig. 9a), the LCL remained nearly constant. Low-level upslope easterly winds were apparent beneath ~1.5 km until the time of CI when downslope westerly flow dominated at all levels. From 1000 to 1200 there was an inversion, or lid, at 1.5–2 km inhibiting convective development. From 1230 to 1330 a lid existed at 3 km. Such warm, dry layers were also observed by BASIL at the Achern Supersite between 1.8 and 3 km (Fig. 6). After 1330 low-level warming ensued, the two layers of capping inversions diminished, and cooling and moistening at 4–5 km combined to allow for CI to occur at 1400.

On the peak of the Vosges Mountains (non-CI location at 1235 m), there was a strong lid of warm air at ~2.5 km capping cooler mountain-top air from 1000 to

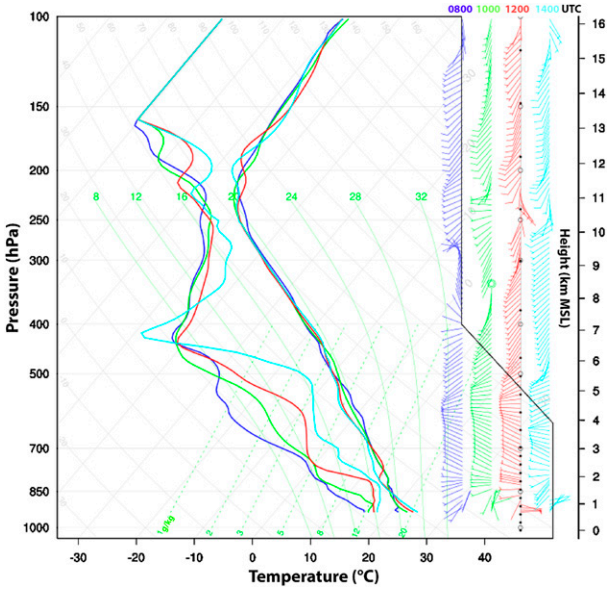

FIG. 8. Simulated sounding time series of dewpoint temperature (left lines), temperature (right lines), and wind profiles from the WRF CI location at 0800 (dark blue), 1000 (green), 1200 (red), and 1400 UTC (light blue) 6 Aug 2007. WRF CI location is shown in Figs. 1, 6c, and 13.

1200 (Fig. 9b). The surface air started to warm at 1200 and the intensity of the 2.5-km lid slightly decreased until 1300 when a new lid at 2 km formed. There were consistently moderate winds (5–7 m s^{-1}) at 3 km and enhanced speed shear beneath 3 km that may have combined with the lids to inhibit the formation of deep convection. Also note that there were no easterly boundary layer winds at the peak so no low-level convergence was established. Thus the small showers that did form were quickly forced off the peak. This is consistent with findings by Kirshbaum (2011).

Figures 9c and 9d show the same data but plotted as difference fields to more clearly illustrate variations in buoyancy of a parcel lifted from the surface. The difference fields depict the surface value of θ_w minus either the θ_w or θ_{ws} at each height aloft. The negative values contribute to CIN and the positive values contribute to CAPE. At the CI location, negative buoyancy dominated up to 2.5 km through 1100 (Fig. 9c). Slight positive buoyancy ensued until 1330 when positive buoyancy clearly increased. This increase in positive buoyancy allowed for CI in the simulations. At the ridgeline there was a time period of positive buoyancy (1215–1400) throughout the depth of the simulation due to the high ridge-top surface temperatures. It is believed that the vertical wind shear, moderate midlevel winds, and lack of low-level convergence combined to inhibit ridge-top CI during that time period.

b. Low-level winds and moisture

1) OBSERVATIONS

The DOW3 2.9° elevation angle scans roughly paralleled the upward sloping Vosges Mountains and covered a depth of 250–500 m. These terrain-parallel slabs (Fig. 10) illustrate the evolution of the reflectivity and upslope/downslope flow evident in the Doppler radial velocity fields in the 1202–1401 period that led to the storm cell shown at 1501 (Figs. 10g,h).

At 1202 the reflectivity field (Fig. 10a) was mostly uniform exhibiting only clear-air return and no apparent organized convective structures. The somewhat stronger radar return over the Vosges Mountains (−5 to 0 dBZ) was presumably due to an increasing concentration of insects caused by the broad low-level convergence and preference of insects not to be lofted upward (Wilson et al. 1994). This interpretation, rather than ground clutter causing the enhanced echo, is supported by a change in the location and intensity of the mountain-top return from 1202 to 1401.

The radial velocity field showed light (~2.5 m s^{-1}) low-level southerly flow in the Rhine Valley (Fig. 10b) increasing to 5 m s^{-1} southerly flow by 1501 (Fig. 10h). Upslope flow was apparent at 1202 (Fig. 10b) extending slightly west of the 500-m contour line. Note the complex intertwining of upslope and downslope flows (positive and negative radial velocities) within the northeast–southwest band of terrain heights to either side of the 500-m contour (Figs. 10b,d). Stronger westerly winds flowing over the Vosges Mountains (~5 m s^{-1}) clearly dominated this band by 1401 (Fig. 10f). Thus there was convergence (as seen in radial gradients of the radial velocities) along the eastern slope prior to cloud formation at 1300 (Figs. 3b and 10d) and it persisted as more convective cells and eventually precipitation formed at 1401 (Figs. 3c and 10e). Convection that initiated above the convergence region along the slopes grew to 55 dBZ and was 13 km deep by 1501. The storm produced a gust front and they both moved eastward into the Rhine Valley (Figs. 10g,h).

Derived dual-Doppler wind and GPS moisture fields were combined in Figs. 11 and 12. The 500-m retrieved winds and surface stations winds are respectively added in blue and red to complement the 1-km winds. The wind fields illustrate the predominant south-southwesterly flow throughout most of the southern Rhine Valley at 1030 and 1100 (Figs. 11a,b). There was weak south-southeasterly flow at 500 m toward and up the slopes of the Vosges Mountains in the region where the deep convection eventually developed. Similarly there was a slight westerly upslope flow into the Black Forest Mountains on the eastern edge of the dual-Doppler box. The vertical velocity field was somewhat noisy but

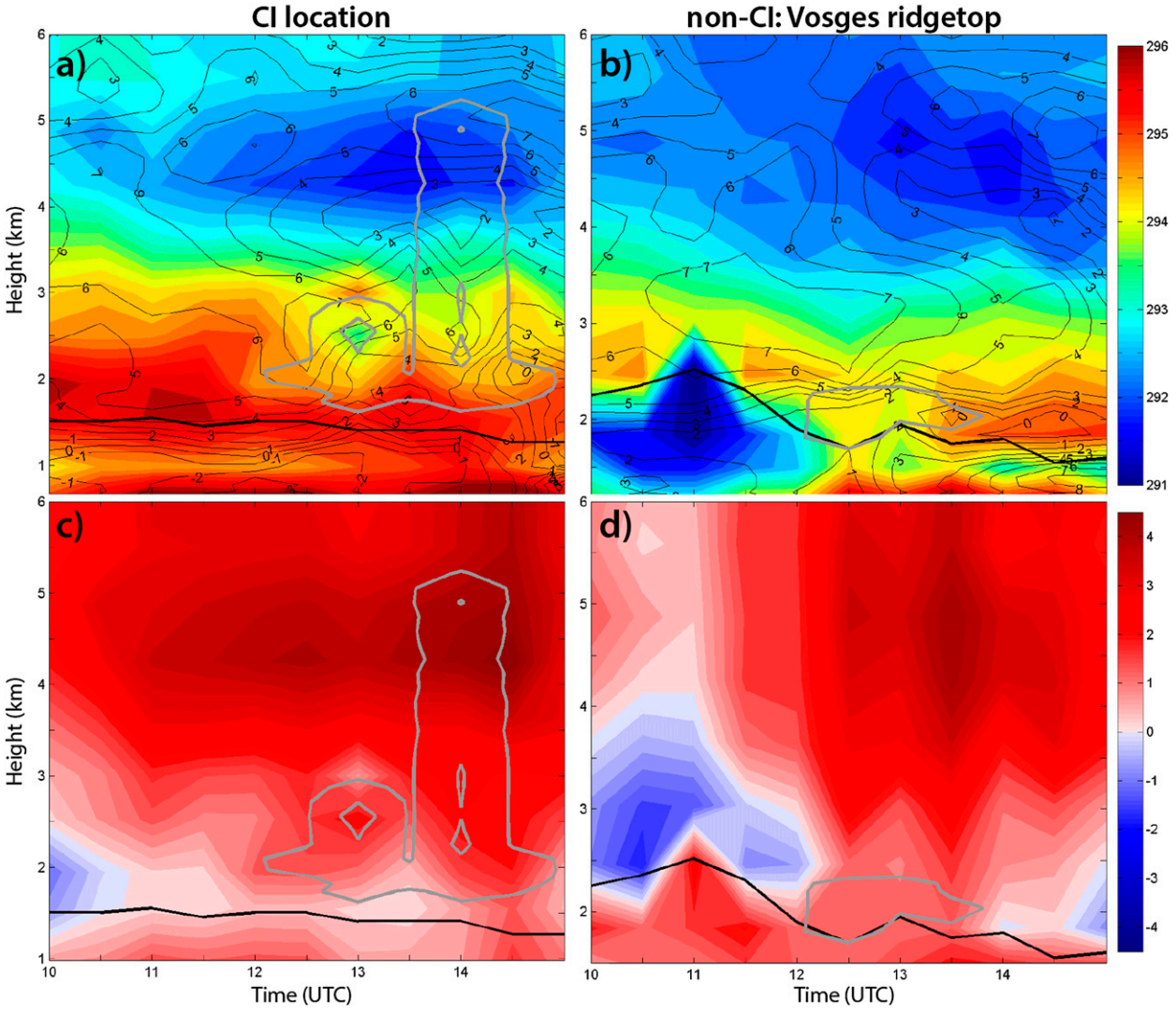

FIG. 9. (a),(b) Time–height plots of simulated wet-bulb potential temperature beneath the LCL (black line) and saturation wet-bulb potential temperature above the LCL. Black contours are u-wind speeds. Gray contours are cloud water mixing ratio values, starting at 0.05 g m^{-3} in increments of 0.5 g m^{-3}. (c),(d) Difference fields of surface wet-bulb potential temperatures minus wet-bulb (or saturated wet-bulb) potential temperatures at the different heights. Profiles are shown at (left) the simulated CI location and (right) a non-CI location at the ridge top of the Vosges Mountains 6.4 km to the west of the CI location.

showed small, weak updrafts that remained over time within the northern Vosges Mountains due to convergence between the northerly winds in that region and the southerly valley and easterly upslope flows. The GPS tomography results at 1 km illustrated relatively dry air throughout the Rhine Valley until 1300 but with enhanced moisture in the northern Vosges Mountains. The observations from 1030 through 1400 (Figs. 11a–e) showed a clear progression of intermittent, small updrafts and likely small clouds (also seen in Fig. 3b), perhaps allowing for the enhancement of moisture through vertical mixing by the continual formation and dissipation of small cells in the region. Eventually, this ever-larger area of updraft and increasing moisture encompassed the observed CI (blue star) shortly after 1400.

The easterly upslope flow persisted at 1200 (Fig. 11c). A weak cyclonic turning of the winds, particularly obvious in the blue vectors at 500 m, was apparent in the southern Rhine Valley and extended from 250 m through 1 km. Additionally there was anticyclonic turning of the westerly winds along the northern edge of the Vosges Mountains to create northwesterly flow. This flow structure around the ends of the mountain barrier was expected from the low Froude number (0.5), indicating that the low-level southwesterly flow should split

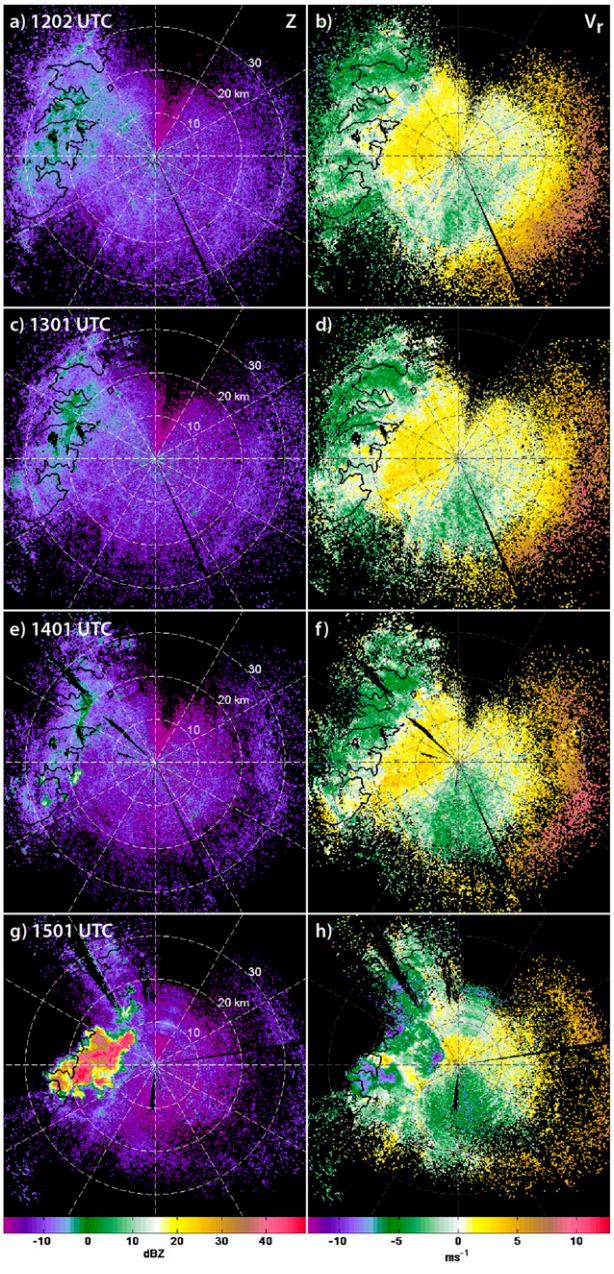

FIG. 10. The 6 Aug 2007 DOW3 radar observations at 2.9° elevation angle: (left) reflectivity (dBZ, scale runs from −10 to +40) and (right) Doppler velocity (m s^{-1}, scale runs from −10 to +10) at (a),(b) 1202, (c),(d) 1301, (e),(f) 1401, and (g),(h) 1501 UTC. Range rings are every 10 km. The 500-m MSL contour is overlaid in black.

around the mountains and is consistent with simulations by Smolarkiewicz and Rotunno (1989).

The east–west vertical cross sections along the latitude of the observed CI show zonal winds and vertical motions in the plane of the figure (Fig. 12). They illustrate weak upslope flow leading to low-level convergence and a broad updraft from $x = -40$ to -20 km between 1100 and 1200. This region also exhibited maximum low-level moisture content (Figs. 12a,b). In addition to the moisture advection over the mountains, there was a daytime upward mixing of the surface moisture shown by the increasing moisture depth throughout the period.

The trend in the moisture distribution continued with persistent dry air throughout the Rhine Valley and a further moisture increase in the northern and central Vosges Mountains, spilling into the northwestern Rhine Valley by 1300 (Fig. 11d). Thus in addition to surface evaporation and vertical mixing apparent from the increased moisture depth in Fig. 12c, this moisture increase appears to be due to advection from the west in advance of the trough. This is consistent with the 8-km VERA moisture fields that showed an enhancement of surface moisture in the Vosges Mountains by 1200 (Fig. 4d) and with the GPS PWV increase along the eastern Vosges between 1200 and 1400 (Figs. 3a–c). The easterly flow further increased into the CI region due to a combination of anabatic winds and the intensification and expansion of the cyclonic circulation in the southern Rhine Valley. The northwesterly flow along the northern Vosges Mountains intensified contributing to a persistent updraft in that region. Figure 12c illustrates enhanced low-level easterlies from $x = -25$ to 5. The bulge in the depth of low-level moisture was coincident with the general region of upward motion along the slopes of the Vosges Mountains (Figs. 12a–c).

The cyclonic circulation in the southern Rhine Valley increased in horizontal extent and magnitude and the northwesterly flow north of the Vosges continued through 1400 when CI occurred. The corresponding low-level convergence and upward vertical velocity expanded and strengthened as the low-level moisture increased by 1400, thereby contributing to CI (Fig. 11e). The vertical cross section (Fig. 12d) shows the enhanced low-level moisture and the updrafts continuing into the core of the new echo. Close examination of the streamlines within numerous vertical cross sections normal to the Vosges Mountains showed the progression of low-level convergence eastward down the slopes through this time period (not shown). The westerly winds in the steering level likely caused the cells to move eastward off the mountains.

By 1500 the storm produced an outflow boundary as shown by the radially outward-directed winds emanating from the radar echo. That gust front exhibited a broad band of updrafts along its leading edge. Both the gust front and the convection had already begun to propagate into the Rhine Valley (Fig. 11f). The associated moisture increased substantially in the Rhine Valley.

The cells intensified as they entered the Rhine Valley and they developed into a north–south-oriented line

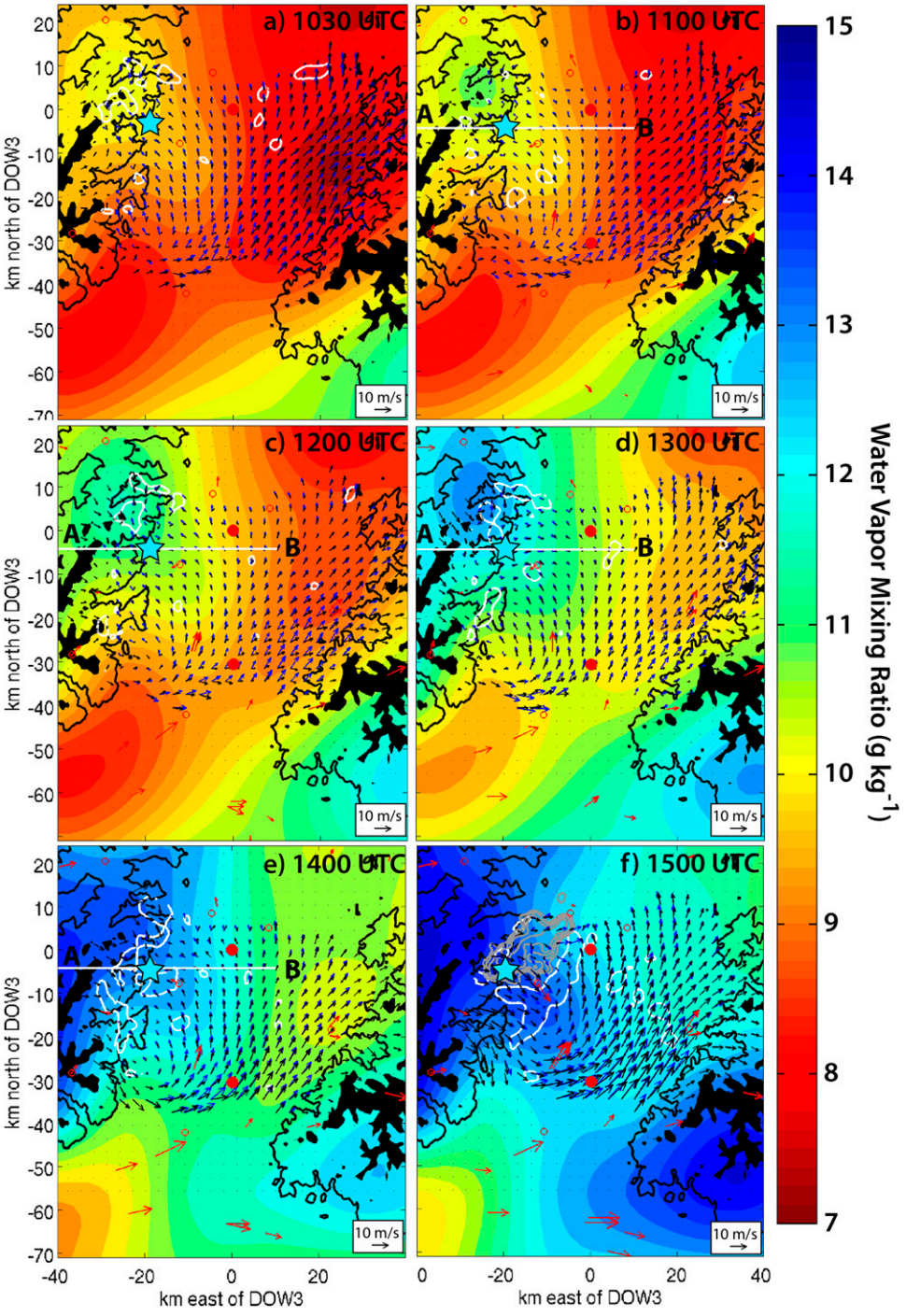

FIG. 11. Dual-Doppler wind vectors and GPS tomography color contours–shading at 1 km MSL from (a) 1030, (b) 1100, (c) 1200, (d) 1300, (e) 1400, and (f) 1500 UTC 6 Aug 2007. Blue vectors are winds at 500 m MSL. The black line is the 500-m MSL terrain contour and black shaded region depicts terrain > 1 km MSL. White contours are updrafts $> 0.3\,\mathrm{m\,s^{-1}}$. Red dots show the locations of the two DOW radars. Red arrows are corresponding surface station wind observations. Blue star shows the observed CI location. Gray contours at 1500 UTC show DOW3 reflectivity every 10 dBZ starting at 10 dBZ. Line A–B indicates the cross-sectional location to be shown in Fig. 12.

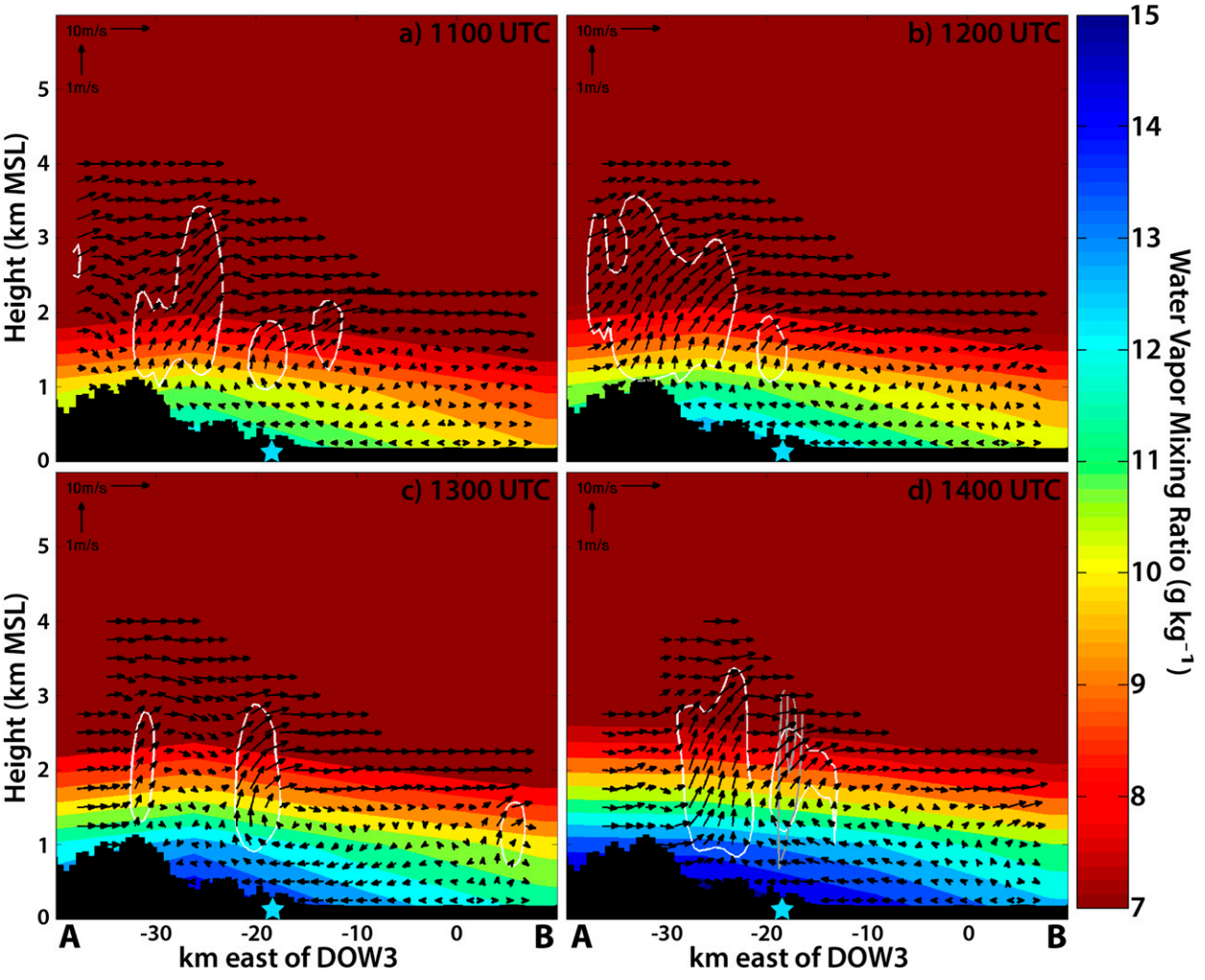

FIG. 12. Dual-Doppler winds and GPS tomography along A–B cross section shown in Fig. 11. Times shown are (a) 1100, (b) 1200, (c) 1300, and (d) 1400 UTC 6 Aug 2007. Color contours–shading are GPS tomographic water vapor mixing ratio fields (g kg^{-1}). Gray contours at 1400 UTC show DOW3 reflectivity every 10 dBZ starting at 10 dBZ. Updrafts > 0.3 m s^{-1} are contoured in white. Blue star at -18 km from DOW3 marks the CI location. Vertical velocity scale is magnified over the horizontal zonal wind scale (shown in the top left of each panel.) Black contours show the terrain.

of thunderstorms (see Fig. 7d). This enhancement is consistent with those found in the climatology of convective enhancements within the Rhine Valley (Weckwerth et al. 2011). In the current case study the further development may be due to enhanced moisture that advected into the Rhine Valley in advance of the frontal-trough system.

2) SIMULATIONS

The WRF simulations (Figs. 13 and 14) suggested flow patterns and convective development similar to those observed (Figs. 11 and 12). The WRF terrain-following surface wind field illustrated the low-level easterly flow moving into the central Vosges Mountains starting at 0700 (not shown). This occurred after solar effects initiated differential heating along the slopes after sunrise at 0355. The inner domain at 1030 and 1100 at 1 km (Figs. 13a,b) showed dry, southwesterly flow throughout the Rhine Valley. There was greater moisture in the northern and central Rhine, consistent with observations. Additionally the northerly flow around the northern Vosges Mountains was reproduced in the simulations. The Froude number calculated at the Nancy location in the simulations was 0.5 and the resulting flow split around the southwestern edge of the Vosges Mountains, as expected.

The east–west vertical cross section through the WRF CI location showed a ~1-km-deep moist layer in the Rhine Valley that extended up to the peak of the Vosges Mountains (Fig. 14a). The WRF simulation showed upslope flow causing shallow updrafts and deepening moisture along the eastern slope of the Vosges Mountains.

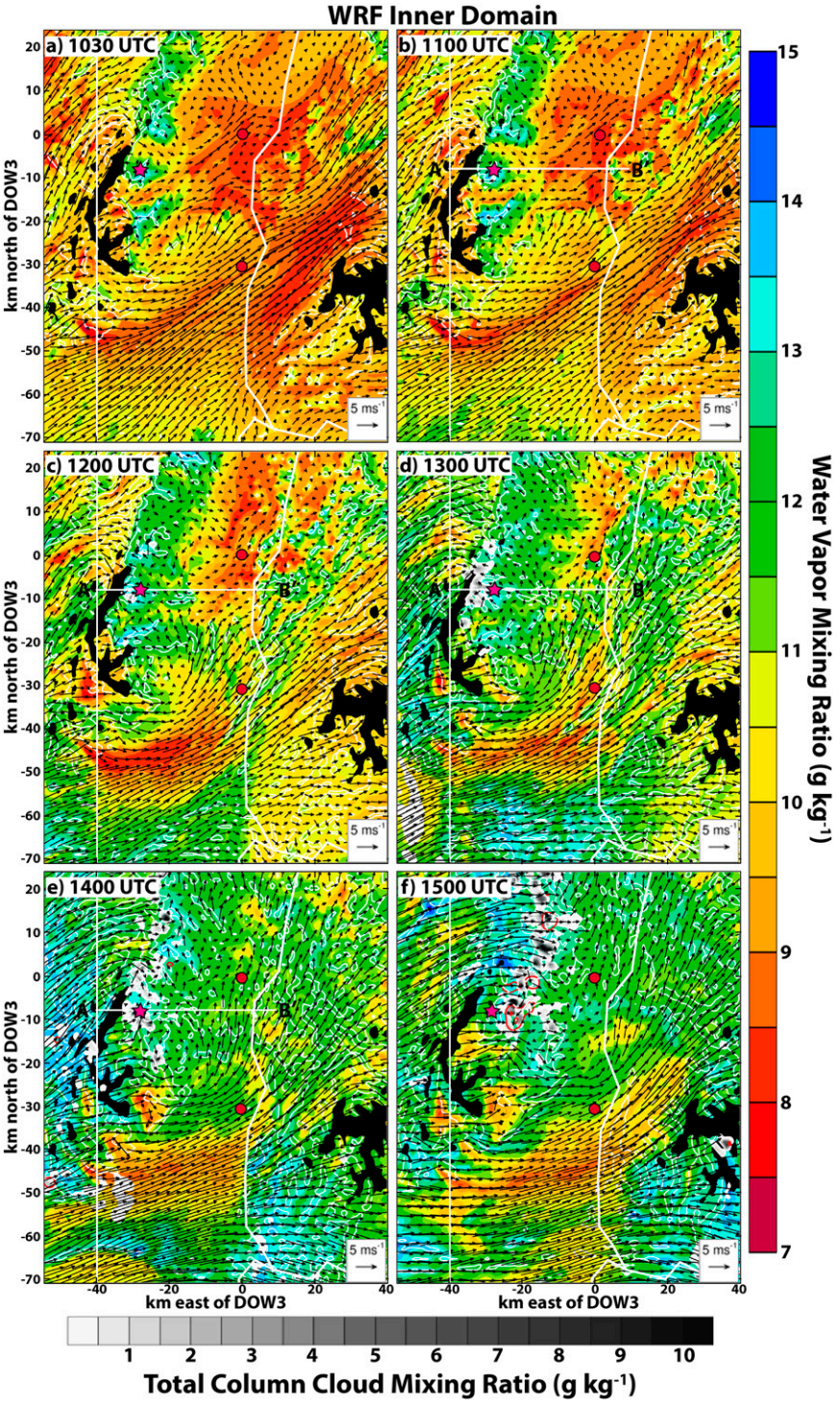

FIG. 13. WRF data plotted on DOW domain of Fig. 11 but extended 10 km west at 1 km MSL for (a) 1030, (b) 1100, (c) 1200, (d) 1300, (e) 1400, and (f) 1500 UTC 6 Aug 2007. Background field of simulated water vapor mixing ratio ($g\,kg^{-1}$) is shown in colored shading along with horizontal wind vectors at 1 km MSL overlaid. White contours are 1 km vertical velocities $> 0.3\,m\,s^{-1}$. Gray shades are the total column cloud water mixing ratio ($g\,kg^{-1}$). Red contours are rainwater mixing ratios $> 0.05\,g\,kg^{-1}$ with increments of $0.5\,g\,kg^{-1}$. Red dots in the Rhine Valley indicate the DOW locations. Pink star is the WRF simulated CI location. The west edge of the dual-Doppler box of Fig. 11 is shown by a vertical white line. Cross sections along A′–B′ will be shown in Fig. 14.

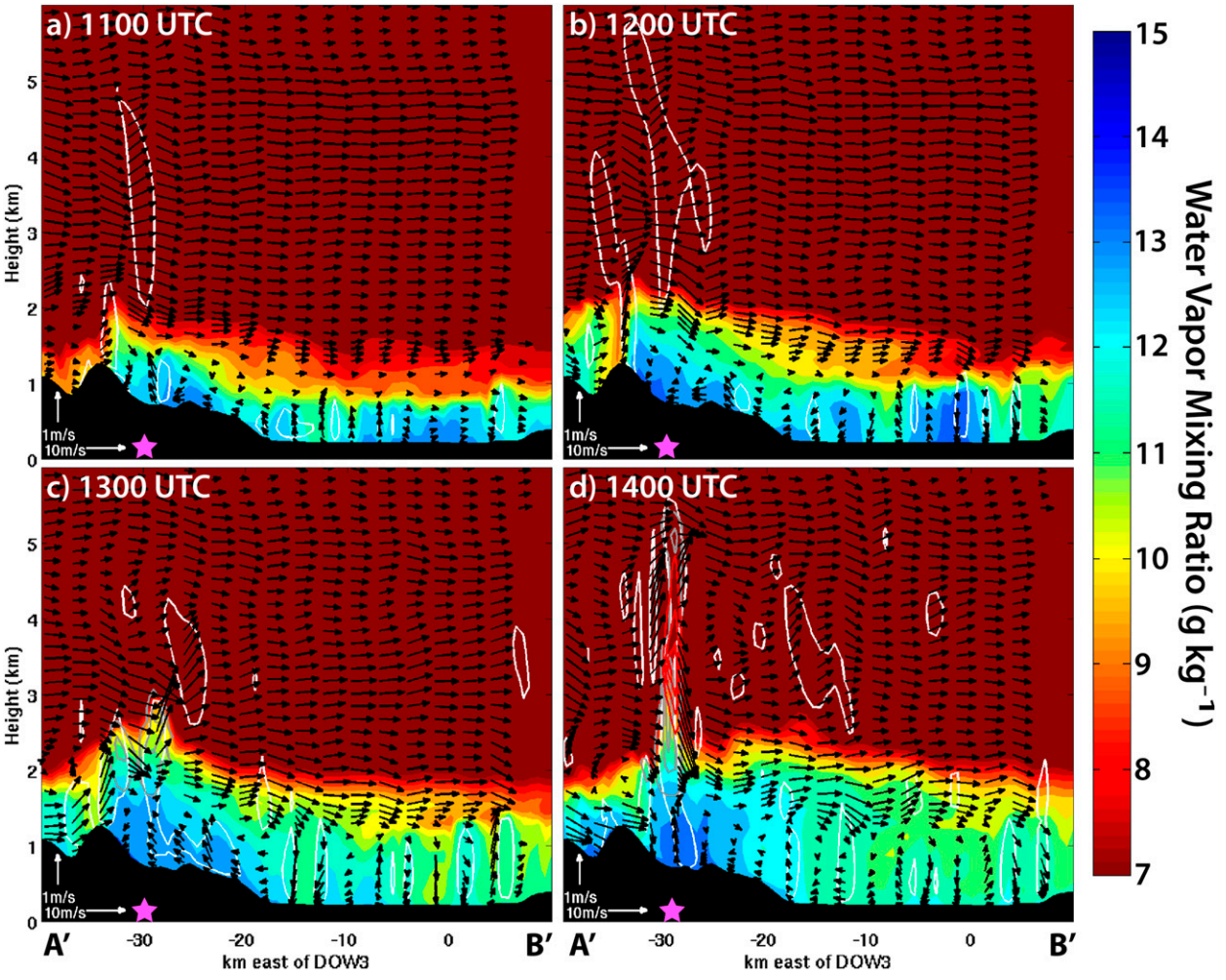

FIG. 14. WRF A′–B′ east–west cross sections along simulated CI location shown in Fig. 13. Results from WRF inner domain are shown for simulation times of (a) 1100, (b) 1200, (c) 1300, and (d) 1400 UTC 6 Aug 2007. Background field of water vapor mixing ratio (colored shading, $g\,kg^{-1}$) is shown along with horizontal wind vectors in the cross section overlaid. Vertical velocities $> 0.3\,m\,s^{-1}$ are contoured in white. Cloud water mixing ratio and rainwater mixing ratio are respectively shown in gray and red in $0.5\,g\,m^{-3}$ contour increments, starting with $0.05\,g\,m^{-3}$. Pink star is the CI location in the WRF simulation. The horizontal zonal wind scale is shown in the bottom left of each panel.

The formation of weak cyclonic flow in the southern Rhine Valley (Fig. 13c) potentially contributed to the low-level upslope flow into the central Vosges Mountains. As the moisture at 1 km increased by horizontal and vertical advection along the central and northern Vosges Mountains, clouds started to form along the slopes. In the vertical cross section, it is apparent that the upslope flow continued at low levels (Fig. 14b). The low-level moisture continued to deepen throughout the cross section.

Because of a combination of differential heating and the northern branch of the cyclonic flow in the southern Rhine Valley, the easterly flow extended farther up the slopes and reached its peak extent and intensity and formed clouds at 1300 (Figs. 13d and 14c). The southwesterly flow in the Rhine Valley increased (Fig. 13d) and the midlevel westerly flow over the Vosges Mountains strengthened (Fig. 14c). Low-level convergence led to updrafts in a similar location, but in a narrower region than observed, and combined with a deepening of the moisture field to produce small clouds at an altitude of 2–2.5 km (Fig. 14c).

The low-level convergence and enhanced moisture coincided with the location and timing of CI at 1400 (Fig. 14d). Moderate westerlies from WRF (Fig. 13e) pushed the clouds and developing storms off the mountains and the storms dissipated in the Rhine Valley at 1500 (Fig. 13f). The simulated storms did not intensify to deep convection, perhaps due to the moderate steering flow forcing it off its persistent updraft and creating an imbalance between the cloud motion and low-level convergence location (e.g., Wilson and Megenhardt 1997;

Kirshbaum 2011). The westerlies in the steering level (2–4 km) were stronger in the simulations than in the observations (cf. Figs. 12 and 14). It is also possible that the interaction between the microphysics and dynamics in the observed storms played a role in the intensity, which WRF was unable to capture.

Many similarities exist between the high-resolution observations and high-resolution simulations. These include upslope flow caused by differential heating along the slopes and cyclonic (anticyclonic) flow in the southern (northern) Rhine Valley. These upslope-generating flow structures caused low-level convergence when they met the large-scale westerly winds along the eastern slopes of the Vosges Mountains. The resulting low-level convergence zone occurred within a region of increasing and deepening moisture due to advection and vertical mixing. This coincided with a region that was unstable to parcel ascent and led to CI in both observations and simulations. The simulations, however, did not allow the storms to develop into deep convection as the moderate westerlies forced the cells off the mountains.

5. Summary and conclusions

The COPS field campaign was conducted in the Rhine Valley bounded on the west by the Vosges and on the east by the Black Forest Mountains. The specific case of CI on 6 August 2007 studied herein occurred along the eastern slopes of the Vosges Mountains in France. Doppler radar and GPS observations were used to obtain four-dimensional wind and water vapor fields during COPS. This is the first known study where such high-resolution wind (250-m vertical and 500-m horizontal) and water vapor (500-m vertical and 16–18 km horizontal) fields have been combined to provide a detailed picture of processes leading to CI in complex terrain. High-resolution WRF numerical simulations (0.7 km) resulted in wind and moisture fields that were remarkably similar to those observed. Furthermore, there was very good agreement between the observed and simulated time and location of CI. The simulations did not produce a storm as strong as that observed but the large- and small-scale conditions were replicated quite well.

The processes important for CI in this case study, labeled schematically in Fig. 15, were found to be due to the following causes:

1) There was development and persistence of convergence along the slopes of the Vosges Mountains as a result of (i) easterly upslope flow converging with the large-scale westerly flow descending over the peaks of the Vosges Mountains; (ii) enhanced easterly upslope flow, partially due to the northern branch of the cyclonic circulation in the southern Rhine Valley; and (iii) northerly low-level flow turning around the northern edge of the Vosges Mountains converging with both the upslope flow and the southerly valley flow.
2) There was a moistening of broad regions by (i) surface evaporation, thermal convection, and boundary layer vertical mixing increasing the depth of the moist layer; (ii) vertical mixing by small clouds forming and dissipating in the region; and (iii) moisture

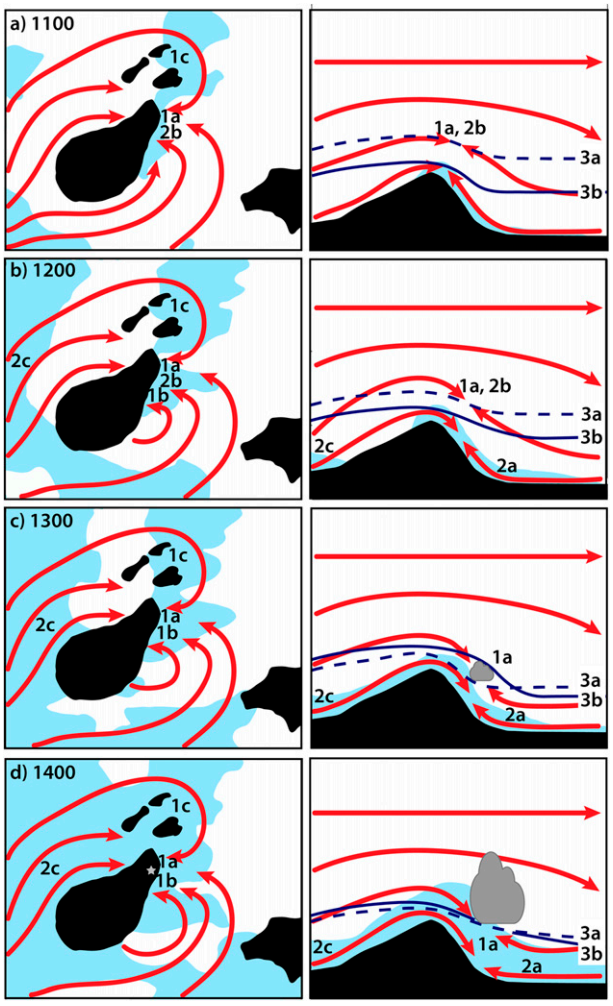

FIG. 15. Schematic summary of results at (a) 1100, (b) 1200, (c) 1300, and (d) 1400 UTC. (left) Horizontal cross sections with streamlines in red and water vapor mixing ratios $> 12\,g\,kg^{-1}$ in blue shades at 700 m MSL. Black regions are terrain > 700 m MSL. Gray star (near top end of black area) in (d) indicates approximate CI location. (right) East–west vertical cross sections along CI location with the red streamlines, blue-shaded water vapor mixing ratios $>12\,g\,kg^{-1}$, and black terrain. Dashed blue line is estimated LCL and solid blue line depicts the lid. The labels are described in section 5 of the text.

advection over the Vosges Mountains in advance of a synoptic-scale frontal-trough system.

3) The WRF simulations suggested that spatial and temporal variability of the (i) LCL and (ii) capping layers, or lids, combined to influence the location and timing of convective development.

These kinematic and thermodynamic processes were observed over a period of 3.5 h as the amount of moisture and its depth increased, creating an area ripe for the initiation of deep, moist convection. High-resolution observations of the low-level wind, moisture, and buoyancy fields were helpful in understanding the CI on this day. This study also showed that high-resolution simulations can reproduce complicated flows in complex terrain and can accurately simulate the timing and location of CI.

This unique combination of 3D winds and moisture fields can be used for multiple purposes, such as for observing the moisture field and moisture advection, which are important for studying and forecasting convective processes. Even higher-resolution observations would be useful in complex terrain to better observe valley flow and moisture variations leading to convective development. Such a combination could be valuable for forecasting potential flash flood events in complex terrain. Further research on combining dual-Doppler winds with high-resolution tomographic retrievals is proposed as part of the Front Range Observational Network Test bed (FRONT) and may be evaluated in the Colorado Front Range in the future.

Acknowledgments. The COPS PIs are gratefully acknowledged for bringing together this rich and diverse dataset. The DOW dataset was collected by the staff of Center for Severe Weather Research (CSWR) through the support of the Deutsche Forschungsgemeinschaft (DFG) and Ministry of Science of Baden-Württemberg, Germany. The VERA analyses were provided by Theresa Gorgas (U. Vienna). The U.K. Facility for Ground-based Atmospheric Measurement (FGAM) wind profiler data were provided by Emily Norton and the Salford lidar data by Fay Davies.

Fruitful discussions with Jim Wilson are much appreciated. Constructive reviews by Wen-Chau Lee and Jim Wilson greatly improved an earlier version of this manuscript. Two anonymous reviewers and Dan Kirshbaum are gratefully acknowledged for their insightful, thorough, and helpful comments.

The second (LJB) and sixth authors (AMB) acknowledge support from the Natural Environment Research Council Grant NE/E018483/1. The fourth author's (JVB) participation in the COPS campaign was financially supported by the ANR (Grant ANR-06-BLAN-0018-04: 648 COPS/France) and CNRS/INSU (LEFE/IDAO program) in France. Support of the last author (TJH) through the NCAR Short-Term Explicit Prediction (STEP) program is greatly appreciated.

REFERENCES

Banta, R. M., 1984: Daytime boundary-layer evolution over mountainous terrain. Part I: Observations of the dry circulations. *Mon. Wea. Rev.,* **112,** 340–356, doi:10.1175/1520-0493(1984)112<0340:DBLEOM>2.0.CO;2.

Behrendt, A., and Coauthors, 2011: Observation of convection initiation processes with a suite of state-of-the-art research instruments during COPS IOP 8b. *Quart. J. Roy. Meteor. Soc.,* **137,** 81–100, doi:10.1002/qj.758.

Bennett, L. J., and Coauthors, 2011: Initiation of convection over the Black Forest Mountains during COPS IOP15a. *Quart. J. Roy. Meteor. Soc.,* **137,** 176–189, doi:10.1002/qj.760.

Bevis, M., S. Businger, T. A. Herring, C. Rocken, R. A. Anthes, and R. H. Ware, 1992: GPS meteorology: Remote sensing of atmospheric water vapour using the global positioning system. *J. Geophys. Res.,* **97,** 15 787–15 801, doi:10.1029/92JD01517.

——, ——, S. R. Chiswell, T. A. Herring, R. A. Anthes, C. Rocken, and R. H. Ware, 1994: GPS meteorology: Mapping zenith wet delay onto precipitable water. *J. Appl. Meteor.,* **33,** 379–386, doi:10.1175/1520-0450(1994)033<0379:GMMZWD>2.0.CO;2.

Bhawar, R., and Coauthors, 2011: The water vapour intercomparison effort in the framework of the Convective and Orographically-induced Precipitation Study: Airborne-to-ground-based and airborne-to airborne lidar systems. *Quart. J. Roy. Meteor. Soc.,* **137,** 325–348, doi:10.1002/qj.697.

Businger, S., and Coauthors, 1996: The promise of GPS in atmospheric monitoring. *Bull. Amer. Meteor. Soc.,* **77,** 5–18, doi:10.1175/1520-0477(1996)077<0005:TPOGIA>2.0.CO;2.

Byers, H. R., and R. R. Braham Jr., 1949: *The Thunderstorm.* U.S. Government Printing Office, 287 pp.

Chaboureau, J. P., F. Guichard, J. L. Redelsperger, and J. L. Lafore, 2004: The role of stability and moisture in the diurnal cycle of convection over land. *Quart. J. Roy. Meteor. Soc.,* **130,** 3105–3117, doi:10.1256/qj.03.132.

Corsmeier, U., and Coauthors, 2011: Processes driving deep convection over complex terrain: A multi-scale analysis of observations from COPS IOP 9c. *Quart. J. Roy. Meteor. Soc.,* **137,** 137–155, doi:10.1002/qj.754.

Cressman, G. P., 1959: An operational objective analysis system. *Mon. Wea. Rev.,* **87,** 367–384, doi:10.1175/1520-0493(1959)087<0367:AOOAS>2.0.CO;2.

Di Girolamo, P., D. Summa, and R. Ferretti, 2009: Multiparameter Raman lidar measurements for the characterization of a dry stratospheric intrusion event. *J. Atmos. Oceanic Technol.,* **26,** 1742–1762, doi:10.1175/2009JTECHA1253.1.

——, ——, R. Bhawar, T. Di Iorio, M. Cacciani, I. Veselovskii, O. Dubovik, and A. Kolgotin, 2012: Raman lidar observations of a Saharan dust outbreak event: Characterization of the dust optical properties and determination of particle size and micropshysical parameters. *Atmos. Environ.,* **50,** 66–78, doi:10.1016/j.atmosenv.2011.12.061.

Gal-Chen, T., 1982: Errors in fixed and moving frames of references: Applications for conventional and Doppler radar analysis. *J. Atmos. Sci.,* **39,** 2279–2300, doi:10.1175/1520-0469(1982)039<2279:EIFAMF>2.0.CO;2.

Geerts, B., Q. Miao, and J. C. Demko, 2008: Pressure perturbations and upslope flow over a heated, isolated mountain. *Mon. Wea. Rev.,* **136,** 4272–4288, doi:10.1175/2008MWR2546.1.

Gorgas, T., M. Dorninger, and R. Steinacker, 2009: High resolution analyses based on the D_PHASE and COPS GTS and non-GTS data set. *Ann. Meteor.,* **44,** 94–95.

Hagen, M., J. van Baelen, and E. Richard, 2011: Influence of the wind profile on the initiation of convection in mountainous terrain. *Quart. J. Roy. Meteor. Soc.,* **137,** 224–235, doi:10.1002/qj.784.

Hane, C. E., C. J. Kessinger, and P. S. Ray, 1987: The Oklahoma squall line of 19 May 1977. Part II: Mechanisms for maintenance of the region of strong convection. *J. Atmos. Sci.,* **44,** 2866–2883, doi:10.1175/1520-0469(1987)044<2866:TOSLOM>2.0.CO;2.

Hanley, K. E., D. J. Kirshbaum, S. E. Belcher, N. M. Roberts, and G. Leoncini, 2011: Ensemble predictability of an isolated mountain thunderstorm in a high-resolution model. *Quart. J. Roy. Meteor. Soc.,* **137,** 2124–2137, doi:10.1002/qj.877.

Kalthoff, N., and Coauthors, 2011: The dependence of convection-related parameters on surface and boundary-layer conditions over complex terrain. *Quart. J. Roy. Meteor. Soc.,* **137,** 70–80, doi:10.1002/qj.686.

Kingsmill, D. E., 1995: Convection initiation associated with a sea-breeze front, a gust front, and their collision. *Mon. Wea. Rev.,* **123,** 2913–2933, doi:10.1175/1520-0493(1995)123<2913:CIAWAS>2.0.CO;2.

Kirshbaum, D. J., 2011: Cloud-resolving simulations of deep convection over a heated mountain. *J. Atmos. Sci.,* **68,** 361–378, doi:10.1175/2010JAS3642.1.

Kottmeier, C., and Coauthors, 2008: Mechanisms initiating deep convection over complex terrain during COPS. *Meteor. Z.,* **17,** 931–948, doi:10.1127/0941-2948/2008/0348.

Labbouz, L., and Coauthors, 2013: Precipitation on the lee side of the Vosges Mountains: Multi-instrumental study of one case from the COPS campaign. *Meteor. Z.,* **22,** 413–432, doi:10.1127/0941-2948/2013/0413.

May, P. T., 1999: Thermodynamic and vertical velocity structure of two gust fronts observed with a wind profiler/RASS during MCTEX. *Mon. Wea. Rev.,* **127,** 1796–1807, doi:10.1175/1520-0493(1999)127<1796:TAVVSO>2.0.CO;2.

Miller, L. J., J. D. Tuttle, and C. K. Knight, 1988: Airflow and hail growth in a severe northern high plains supercell. *J. Atmos. Sci.,* **45,** 736–762, doi:10.1175/1520-0469(1988)045<0736:AAHGIA>2.0.CO;2.

——, ——, and G. B. Foote, 1990: Precipitation production in a large Montana hailstorm: Airflow and particle growth trajectories. *J. Atmos. Sci.,* **47,** 1619–1646, doi:10.1175/1520-0469(1990)047<1619:PPIALM>2.0.CO;2.

Mohr, C. G., L. J. Miller, R. L. Vaughan, and H. W. Frank, 1986: The merger of mesoscale datasets into a common Cartesian format for efficient and systematic analysis. *J. Atmos. Oceanic Technol.,* **3,** 143–161, doi:10.1175/1520-0426(1986)003<0143:TMOMDI>2.0.CO;2.

Morcrette, C., H. Lean, K. Browning, J. Nicol, N. Roberts, P. Clark, A. Russell, and A. Blyth, 2007: Combination of mesoscale and synoptic mechanisms for triggering an isolated thunderstorm: Observational case study of CSIP IOP 1. *Mon. Wea. Rev.,* **135,** 3728–3749, doi:10.1175/2007MWR2067.1.

Neiman, P. J., F. M. Ralph, A. B. White, D. E. Kingsmill, and P. O. G. Persson, 2002: The statistical relationship between upslope flow and rainfall in California's coastal mountains: Observations during CALJET. *Mon. Wea. Rev.,* **130,** 1468–1492, doi:10.1175/1520-0493(2002)130<1468:TSRBUF>2.0.CO;2.

O'Brien, J. J., 1970: Alternative solutions to the classical vertical velocity problem. *J. Appl. Meteor.,* **9,** 197–203, doi:10.1175/1520-0450(1970)009<0197:ASTTCV>2.0.CO;2.

Oye, R., C. Mueller, and S. Smith, 1995: Software for radar translation, visualization, editing, and interpolation. Preprints, *27th Conf. on Radar Meteorology,* Vail, CO, Amer. Meteor. Soc., 359–361.

Purdom, J. F. W., and K. Marcus, 1982: Thunderstorm trigger mechanisms over the southeast U.S. Preprints, *12th Conf. on Severe Local Storms,* San Antonio, TX, Amer. Meteor. Soc., 487–488.

Rotach, M. W., and Coauthors, 2009a: MAP D-PHASE: Real-time demonstration of weather forecast quality in the Alpine region. *Bull. Amer. Meteor. Soc.,* **90,** 1321–1336, doi:10.1175/2009BAMS2776.1.

——, and Coauthors, 2009b: Supplement to MAP D-PHASE: Real-time demonstration of weather forecast quality in the Alpine region: Additional applications of the D-Phase datasets. *Bull. Amer. Meteor. Soc.,* **90,** S28–S32, doi:10.1175/2009BAMS2776.2.

Skamarock, W. C., and Coauthors, 2008: A description of the Advanced Research WRF version 3. NCAR Tech. Rep. NCAR/TN-475+STR, 113 pp., doi:10.5065/D68S4MVH.

Smolarkiewicz, P., and R. Rotunno, 1989: Low Froude number flow past three-dimensional obstacles. Part I: Baroclinically generated lee vortices. *J. Atmos. Sci.,* **46,** 1154–1164, doi:10.1175/1520-0469(1989)046<1154:LFNFPT>2.0.CO;2.

Steinacker, R., C. Häberli, and W. Pöttschacher, 2000: A transparent method for the analysis and quality evaluation of irregularly distributed and noisy observational data. *Mon. Wea. Rev.,* **128,** 2303–2316, doi:10.1175/1520-0493(2000)128<2303:ATMFTA>2.0.CO;2.

——, and Coauthors, 2006: A mesoscale data analysis and downscaling method over complex terrain. *Mon. Wea. Rev.,* **134,** 2758–2771, doi:10.1175/MWR3196.1.

Van Baelen, J., J.-P. Aubagnac, and A. Dabas, 2005: Comparison of near-real-time estimates of integrated water vapour derived with GPS, radiosondes, and microwave radiometer. *J. Atmos. Oceanic Technol.,* **22,** 201–210, doi:10.1175/JTECH-1697.1.

——, M. Reverdy, F. Tridon, L. Labbouz, G. Dick, M. Bender, and M. Hagen, 2011: On the relationship between water vapour field evolution and the life cycle of precipitation systems. *Quart. J. Roy. Meteor. Soc.,* **137,** 204–223, doi:10.1002/qj.785.

Wang, J., H. L. Cole, D. J. Carlson, E. R. Miller, K. Beierle, A. Paukkunen, and T. K. Laine, 2002: Corrections of humidity measurement errors from the Vaisala RS80 radiosonde—Application to TOGA-COARE data. *J. Atmos. Oceanic Technol.,* **19,** 981–1002, doi:10.1175/1520-0426(2002)019<0981:COHMEF>2.0.CO;2.

——, L. Zhang, A. Dai, T. Van Hove, and J. Van Baelen, 2007: A near-global two-hourly data set of atmospheric precipitable water from ground-based GPS measurements. *J. Geophys. Res.,* **112,** D11107, doi:10.1029/2006JD007529.

Weckwerth, T. M., J. W. Wilson, M. Hagen, T. J. Emerson, J. O. Pinto, D. L. Rife, and L. Grebe, 2011: Radar climatology of the COPS region. *Quart. J. Roy. Meteor. Soc.,* **137,** 31–41, doi:10.1002/qj.747.

Wilson, J. W., and W. E. Schreiber, 1986: Initiation of convective storms at radar-observed boundary-layer convergence lines. *Mon. Wea. Rev.,* **114,** 2516–2536, doi:10.1175/1520-0493(1986)114<2516:IOCSAR>2.0.CO;2.

——, and C. K. Mueller, 1993: Nowcasts of thunderstorm initiation and evolution. *Wea. Forecasting,* **8,** 113–131, doi:10.1175/1520-0434(1993)008<0113:NOTIAE>2.0.CO;2.

——, and D. L. Megenhardt, 1997: Thunderstorm initiation, organization, and lifetime associated with Florida boundary layer convergence lines. *Mon. Wea. Rev.,* **125,** 1507–1525, doi:10.1175/1520-0493(1997)125<1507:TIOALA>2.0.CO;2.

——, T. M. Weckwerth, J. Vivekanandan, R. M. Wakimoto, and R. W. Russell, 1994: Boundary layer clear-air radar echoes: Origin of echoes and accuracy of derived winds. *J. Atmos. Oceanic Technol.,* **11,** 1184–1206, doi:10.1175/1520-0426(1994)011<1184:BLCARE>2.0.CO;2.

Wulfmeyer, V., and Coauthors, 2008: The Convective and Orographically Induced Precipitation Study: A research and development project of the World Weather Research Program for improving quantitative precipitation forecasting in low-mountain regions. *Bull. Amer. Meteor. Soc.,* **89,** 1477–1486, doi:10.1175/2008BAMS2367.1.

——, and Coauthors, 2011: The Convective and Orographically-induced Precipitation Study (COPS): The scientific strategy, the field phase and first highlights. *Quart. J. Roy. Meteor. Soc.,* **137,** 3–30, doi:10.1002/qj.752.

Wurman, J., J. Straka, E. Rasmussen, M. Randall, and A. Zahrai, 1997: Design and deployment of a portable, pencil-beam, pulsed, 3-cm Doppler radar. *J. Atmos. Oceanic Technol.,* **14,** 1502–1512, doi:10.1175/1520-0426(1997)014<1502:DADOAP>2.0.CO;2.